# Contribution of mesoscale processes to nutrient budgets in the Arabian Sea

Laure Resplandy, Marina Lévy, Gurvan Madec, Stéphane Pous, Olivier Aumont, D. Kumar

# Contribution of mesoscale processes to nutrient budgets in the Arabian Sea

L. Resplandy,[1] M. Lévy,[1] G. Madec,[1,2] S. Pous,[1] O. Aumont,[3] and D. Kumar[4]

Received 4 February 2011; revised 3 August 2011; accepted 4 August 2011; published 5 November 2011.

[1] We examine the impact of mesoscale dynamics on the seasonal cycle of primary production in the Arabian Sea with an eddy-resolving (1/12°) bio-physical model. Comparison with observations indicates that the numerical model provides a realistic description of climatological physical and biogeochemical fields as well as their mesoscale variability during the Southwest and Northeast Monsoons. We show that mesoscale dynamics favors biological production by modulating the nutrient supplies throughout the year. Different processes are involved depending on the blooming season. During the summer bloom period, we found that the main process is the export of nutrients from coastal upwelling regions into the central Arabian Sea by mesoscale filaments. Our model suggests that lateral advection accounts for 50–70% of the total supply of nutrients to the central AS. A less expected result is the major input of nutrients (up to 60–90%) supplied to upwelling regions during the early stage of the summer bloom period by eddy-induced vertical advection. During the winter bloom period, our model evidences for the first time how vertical velocities associated with mesoscale structures increase the supply of nutrients to the upper layer by 40–50% in the central Arabian Sea. Finally, the restratification effect of mesoscale structures modulates spatially and temporally the restratification that occurs at large-scale at the end of the Northeast Monsoon. Although this effect has no significant impact on the large-scale budget, it could be a source of uncertainty in satellite and in-situ observations.

**Citation:** Resplandy, L., M. Lévy, G. Madec, S. Pous, O. Aumont, and D. Kumar (2011), Contribution of mesoscale processes to nutrient budgets in the Arabian Sea, *J. Geophys. Res.*, *116*, C11007, doi:10.1029/2011JC007006.

## 1. Introduction

[2] A singularity of the Arabian Sea (AS) is that the seasonal cycle of phytoplankton is characterized by two blooming periods [*Banse*, 1987] forced by the semi-annual monsoonal wind forcing [*Wiggert et al.*, 2005]. During the summertime Southwest Monsoon, coastal upwelling produces high biological production along the western [*Brock and McClain*, 1992; *Veldhuis et al.*, 1997; *Hitchcock et al.*, 2000] and eastern [*Banse*, 1968; *Lierheimer and Banse*, 2002] coasts of the AS, whereas during the wintertime Northeast Monsoon convective mixing entrains nutrients and increases the biological activity north of 15°N [*Madhupratap et al.*, 1996].

[3] It is now fairly well established that the large-scale spatial distribution of these seasonal blooms is modulated by the numerous mesoscale structures that populate the AS (eddies and filaments). Such structures, observed in ADCP surveys [*Flagg and Kim*, 1998] and by altimetry [*Manghnani et al.*, 1998; *Kim et al.*, 2001; *Fischer et al.*, 2002], have been documented in various studies and review [*Brock et al.*, 1991; *Schott and McCreary*, 2001; *Bower et al.*, 2002; *Brandt et al.*, 2003; *Al Saafani et al.*, 2007]. In particular during the JGOFS 'Arabian Sea process study' program [*Smith et al.*, 1998], a mooring and a sediment trap deployed in the central AS captured major modifications of the mixed layer depth, the chlorophyll concentration and the particle flux associated with open-ocean eddies events [*Dickey et al.*, 1998; *Marra et al.*, 1998; *Honjo et al.*, 1999]. In addition, patches of enhanced chlorophyll and extremely thin mixed layers were sampled within a filament of upwelled water ~500 km offshore the Omani coast [*Brink et al.*, 1998; *Flagg and Kim*, 1998; *Lee et al.*, 2000].

[4] Previous modeling studies at eddy-permitting resolution (only marginally resolving the mesoscale) reproduced the major biological features [*McCreary et al.*, 1996; *Kawamiya and Oschlies*, 2003; *Olascoaga et al.*, 2005; *Wiggert et al.*, 2006; *Koné et al.*, 2009]. One recurrent bias found in those model results was the underestimation of primary production in the central AS. The misrepresentation of the ecosystem complexity (phytoplankton, zooplankton, bacterial loop and nutrients), of the diurnal cycle and of the mesoscale dynamics were invoked to explain this discrepancy [*Kawamiya and Oschlies*, 2003; *Wiggert et al.*, 2005, 2006; *Koné et al.*, 2009]. The analysis based on model comparison by *Friedrichs et al.* [2006] however strongly

[1]LOCEAN, CNRS, IRD, UPMC, MNHN, IPSL, Paris, France.
[2]National Oceanography Centre, Southampton, Southampton, UK.
[3]LPO, CNRS, IRD, Plouzané, France.
[4]National Institute of Oceanography, Dona Paula, India.


0148-0227/11/2011JC007006

suggested that the accuracy of physical forcings and dynamical fields is the major factor that modulates the biogeochemical response in the Arabian Sea. The regional model of *Kawamiya* [2001] supported these findings and showed that the lateral export of nutrients into the central AS during the Southwest Monsoon was intensified when switching from coarse (1°) to eddy-permitting (1/3°) resolution.

[5] In this context, the aim of this paper is to improve the understanding of the mechanisms regulating the seasonal blooms by examining the mesoscale contribution to the nutrient transport. To that purpose, we developed a regional eddy-resolving model, with higher horizontal resolution (1/12°) than in previous bio-physical models of the AS. The main outcome of the paper is a comprehensive description of the mesoscale processes that promote the phytoplankton blooms during the Southwest and the Northeast Monsoons by enhancing the nutrient supply to the upper layer.

[6] The paper is structured as follows: section 2 describes the physical and biogeochemical models. Section 3 evaluates the eddy-resolving model solution against available observations. The model evaluation is complemented by the description of the blooms and mesoscale structures temporal evolution in section 4. The contribution of mesoscale dynamics to the nutrient transport is then estimated in section 5 by using the Reynolds averaging method that allows the distinction between the mean and the eddy-induced advective transports. Section 6 gives a synthesis of the identified mechanisms regulating the blooms during both seasons and puts our results in perspective. Finally, major results are summarized in the conclusion.

## 2. Model and Observations

### 2.1. Physical Model

[7] The model configuration is based on the primitive equation ocean general circulation model NEMO [*Madec*, 2008]. An isotropic Mercator horizontal grid covers the northern Indian Ocean between 5°S and 27°N with 46 vertical levels increasing from 6 m at the surface to 250 m at depth. Both the Bay of Bengal and Arabian Sea are covered by the model, but only results from the Arabian Sea are presented in this study. The bottom cell thickness is calculated using the partial step method [*Pacanowski and Gnanadesikan*, 1998] and adapted to the Etopo2 bathymetry except on continental shelves where the Gebco bathymetry is used [*Molines et al.*, 2006]. The horizontal grid resolution is 1/12° (~9 km), which is smaller than the third baroclinic Rossby radii over the model domain [*Chelton et al.*, 1998]. The model can therefore be considered as eddy-resolving. One of the major challenges is to ensure the model stability in the highly energetic western boundary current and the associated anticyclonic gyre called the Great Whirl, without using excessive momentum dissipation that would damp small-scale processes elsewhere. Momentum, temperature and salinity are therefore advected using a third order diffusive Upstream-Biased Scheme [*Shchepetkin and McWilliams*, 2005; *Madec*, 2008]. The intrinsic diffusivity of this scheme is proportional to the current velocity $u$ ($\frac{1}{12}\Delta x^3|u|$, with $\Delta x$ the horizontal resolution in m). The resulting dissipation is of the order of $6.10^{10}$ $m^4.s^{-1}$ in the Great Whirl (where currents reach 1 $m.s^{-1}$) and 2 orders of magnitude lower in the central Arabian Sea (where currents are of the order of 1 $cm.s^{-1}$). This scheme does not require any additional dissipation and diffusivity to ensure numerical stability. Vertical mixing is modeled with a prognostic turbulent kinetic energy scheme, with background vertical diffusion and viscosity of $10^{-5}$ $m^2.s^{-1}$ and $10^{-4}$ $m^2.s^{-1}$, respectively [*Blanke and Delecluse*, 1993; *Madec*, 2008]. In case of static instability, vertical viscosity and diffusivity are raised to 10 $m^2.s^{-1}$. Quadratic bottom friction is introduced as a boundary stress [*Willebrand et al.*, 2001]. Simulations are performed with no-slip lateral boundary conditions [*Penduff et al.*, 2009]. The diurnal cycle is accounted for by computing a diurnally varying surface short wave flux from the daily mean value [*Bernie et al.*, 2007].

[8] Northern, eastern and western boundaries are closed by continental masses. The southern boundary (5°S) is a radiative open boundary [*Treguier et al.*, 2001], constrained with a 150 days time-scale relaxation to the monthly meridional velocities, temperature and salinity of the interannual global 1/4° simulation DRAKKAR025-G70 [*Barnier et al.*, 2006]. The impact of open boundary conditions is limited by a sponge layer with increasing horizontal viscosity between 3°S and 5°S. The straits of Bab el Mandeb, Hormuz and Malacca are closed and damped in temperature and salinity toward the Levitus climatology [*Levitus et al.*, 1998] with a 10 days time scale.

[9] The initial state is at rest. Temperature and salinity are initialized with the Levitus climatology. The model is forced with the interannual hybrid DRAKKAR Forcing Set 4 (DFS4) extensively described by *Brodeau et al.* [2009]. DFS4 combines CORE formulations [*Large and Yeager*, 2004] with ERA40 turbulent variables (wind, humidity and air temperature), satellite data for radiations and precipitation [*Zhang et al.*, 2004; *Griffies et al.*, 2009]. Both components of the radiative heat flux are computed daily using the longwave and shortwave components of the downwelling radiation, a fixed surface albedo and the sea surface temperature (SST) [*Brodeau et al.*, 2009]. Climatological runoff compiled for the Mercator project are used [*Bourdallé-Badie and Treguier*, 2006]. Surface salinity restoring to the Levitus climatology is performed with a time scale of 300 days for a MLD of 50 m.

### 2.2. Biogeochemical Model

[10] The AS covers inshore nutrient-rich habitats where large size-classes phytoplankton such as diatoms dominate and more oligotrophic regions where small size-classes phytoplankton such as dinoflagellates dominate [*Banse*, 1994; *Garrisonet al.*, 1998]. In order to account for this diversity, we used the intermediate complexity biogeochemical model Pelagic Interaction Scheme for Carbon and Ecosystem Studies (PISCES) that includes two phytoplankton size-classes corresponding to diatoms and nanophytoplankton and two zooplankton size-classes [*Aumont et al.*, 2003; *Aumont and Bopp*, 2006]. Previous model studies suggested that iron and phosphate limitations are marginal in the AS [*Aumont et al.*, 2003; *Moore et al.*, 2004; *Dutkiewicz et al.*, 2005; *Koné et al.*, 2009]. This result is in apparent contradiction with the model simulation of *Wiggert et al.* [2006] and in-situ observations of *Moffett et al.* [2007] that indicate an iron limitation in the Arabian Sea. However the iron limitation over the Arabian Sea is low in the PISCES model *Koné et al.* [2009] and its inclusion in sensitivity

experiments showed only a weak influence on the ecosystem response. Therefore, the original version of PISCES was simplified from 24 to 16 tracers, taking out compartments related to the cycling of phosphate and iron. In this model version, the small size-class phytoplankton is thus limited by nitrogen, while the large size-class corresponding to diatoms is subjected to a nitrogen-silicate colimitation. For phytoplankton, prognostic variables are total biomass, chlorophyll and silicon contents. This means that the Chl:C and Si:C ratios of both phytoplankton groups are fully predicted by the model (Tables A1 and A2 in Appendix A). For all species, the C:N ratio is constant and set to 122/16 [*Takahashi et al.*, 1985]. To ensure positive values, biogeochemical tracers are advected with the positive Monotone Upstream-centered Schemes for Conservation Laws [*Van Leer*, 1979; *Lévy et al.*, 2001] and dissipated along isopycnals at small scales by a laplacian operator with a diffusion coefficient of 100 $m^2.s^{-1}$.

[11] Phytoplankton growth in the PISCES model is parameterized for daily mean insolation values. In the biogeochemical model, we therefore used the daily mean short wave flux and not the diurnally varying flux computed for the dynamical model. Nevertheless, the biogeochemical tracers are subjected to diurnal variations (dilution effect) associated with the diurnal cycle of the mixed-layer.

[12] The initial distribution and the southern open boundary conditions for nitrate, oxygen and dissolved organic carbon were provided by the global monthly climatology derived from the 1/2° simulation of *Koné et al.* [2009]. The other biological tracers were initially set to low values. Annual river discharge of carbon is taken from the Global Erosion Model of *Ludwig et al.* [1996]. Nitrogen and silicate supplies by rivers are derived from the same model using constant N/Si/C ratios [*Koné et al.*, 2009]. However, the Arabian Sea has experienced an abrupt decrease in runoff of ~80% over the last 50 years due to large-scale hydraulic engineering and irrigation [*Kravtsova et al.*, 2009]. The impact of river input is therefore relatively limited in amplitude and mostly confined to coastal areas. As for temperature and salinity, nitrate, oxygen and dissolved organic carbon were damped in the Bab el Mandeb, Hormuz and Malacca straits (see section 2.1). The biogeochemical model formulation and parameters are summarized in Appendix A.

[13] The physical and ecosystem models were integrated from 1992 to 2003. This paper focuses on the analysis of the mean seasonal cycle of the model climatology build by averaging from the fourth (1995) to the thirteenth (2003) year of simulation and over the AS between 42–80°E and 0–27°N. Over this period, the model has not reached full equilibrium. A weak mean drift in nitrate content of $-0.05$ $mmol.m^{-3}.yr^{-1}$ is found in the upper 200 m between 1995 and 2003.

### 2.3. Observations

[14] The model is evaluated against the following climatologies: the climatology of *Lumpkin and Garraffo* [2005] based on drifters observations collected between 1998 and 2003 is used for surface currents. The climatology derived from the Tropical Rainfall Measuring Mission Microwave Imager satellite sensor (TMI, available online at www.remss.com) is used for SST. The 1° resolution climatology of *de Boyer Montégut et al.* [2004] based on observations collected between 1941 and 2008 (available online at http://www.lodyc.jussieu.fr/~cdblod/mld.html) is used for the mixed layer depth (MLD). The MLD in the observation and the data are estimated with a temperature criterion corresponding to an decrease of 0.2°C compared to the temperature at 10 m depth.

[15] To evaluate the strength of mesoscale activity, we used the standard deviation of the band-pass filtered (14–120 days) sea level anomaly (SLA) from the Aviso database (http://www.aviso.oceanobs.com/).

[16] A weekly climatology of SeaWiFS (Sea-viewing Wide Field-of-view Sensor Data) surface chlorophyll *a* (Chl) level-3 binned data at 9 km resolution, available through the OceanColor website (http://oceancolor.gsfc.nasa.gov), has been created between January 1998 and December 2003 (overlapping period of the model and SeaWiFS). Chl during the Southwest monsoon is, however, only sparsely sampled by ocean color satellites due to an intense cloud cover. Observed climatological nitrate concentrations are from the Indian Ocean Hydrobase from *Kobayashi and Suga* [2006].

## 3. Model Evaluation

[17] We examine here how the seasonal wind reversal forces a strong semiannual cycle of the large-scale circulation and mixed layer depth (MLD), which in turn strongly modulates the temperature, the nutrient distribution and the biological production. Results present the dynamical and biogeochemical typical spatial patterns associated with the Northeast Monsoon (December-February, noted NEM) and Southwest Monsoon (June-August, SWM) periods. We then evaluate the model ability at reproducing the mesoscale variability that modulates the dynamics in the AS. The spatial distribution of the biological production is evaluated using the chlorophyll-a concentration, which is very similar to the phytoplankton concentration and can be compared to satellite ocean color products.

### 3.1. Northeast Monsoon

[18] During the NEM period, relatively strong, cool and dry winds blow to the southwest across the AS. These winds force a counterclockwise circulation characterized by the West India Coastal Current (WICC) and the Somali Current (SC). The WICC flows northward off India, whereas the SC flows southward along the coast of Somalia (Figure 1a). NEM winds also induce a strong ocean heat loss in the northern AS, resulting in intense convective mixing [*Bauer et al.*, 1991; *Weller et al.*, 2002]. The signature of this convective mixing is the deepening of the MLD in the northwest [*Rao et al.*, 1989; *Lee et al.*, 2000] (Figure 1b), entraining cold (Figure 1c), nutrient-rich waters (Figure 1d) at the surface and triggering a phytoplankton bloom (Figure 1e).

[19] The model reproduces these large-scale general features. Mixing seems however too intense particularly north of 15°N, where the MLD is 20 to 30 m deeper than in the observations (Figures 1b and 1g). Vertical mixing in this region is highly sensitive to the subsurface water density. We believe that part of the bias could be due to the presence of too light subsurface waters in our model. This is probably

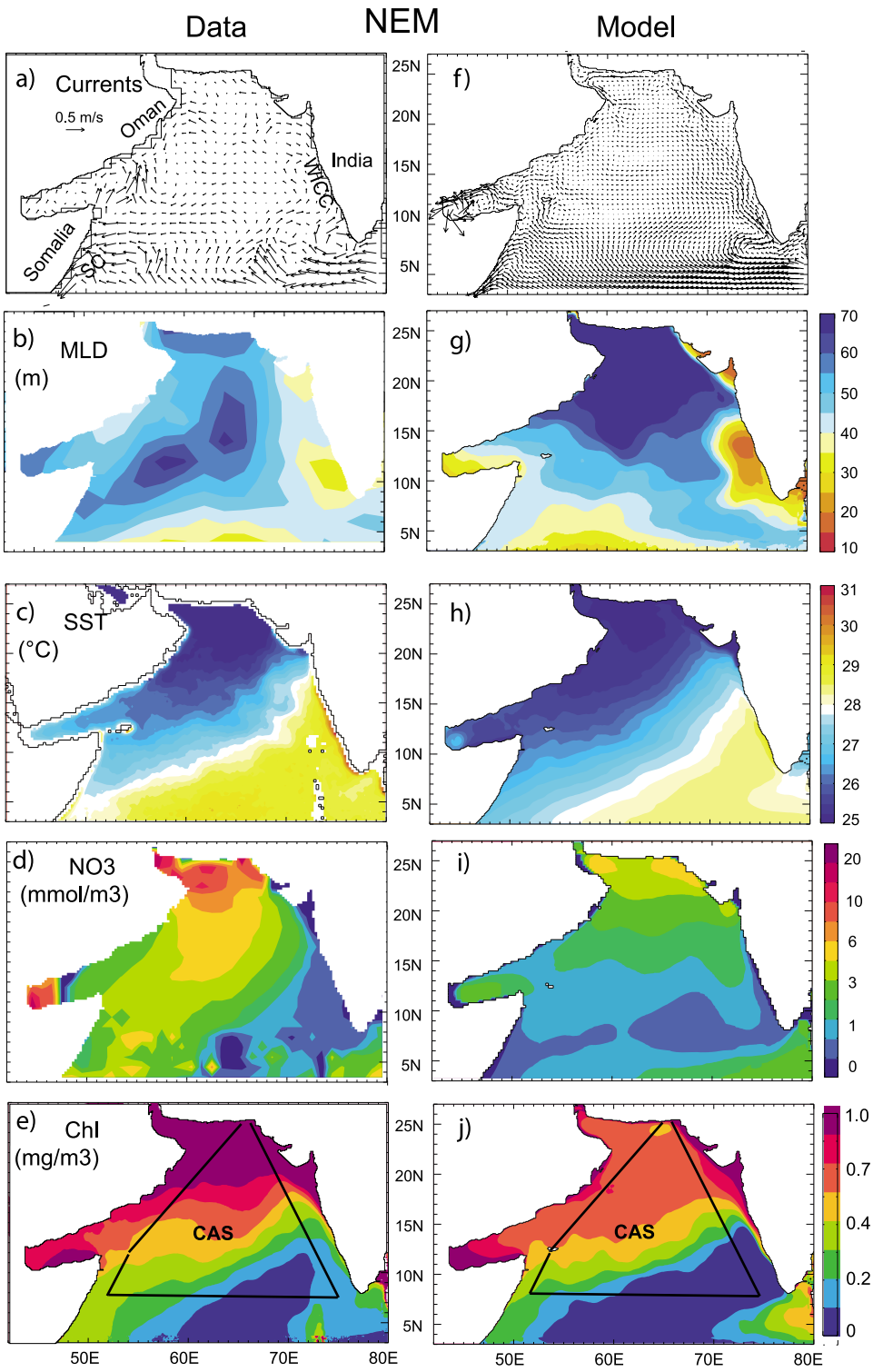


**Figure 1.** Climatological maps of dynamical and biogeochemical properties during the NEM period (Dec-Feb) from (a–e) observations and (f–j) model results. Figure 1a and 1f show currents: SC and WICC refer to the Somali Current and Western Indian Coastal Current respectively. Figures 1b and 1g show mixed-layer depth (MLD, in m) estimated with a temperature threshold of 0.2°C. Figures 1c and 1h show sea surface temperature (SST, in °C). Figures 1d and 1i show nitrate concentration (in $mmol.m^{-3}$) averaged over the upper 80m. Figures 1e and 1j show surface chlorophyll (Chl, in $mg.m^{-3}$). The black line in Figures 1e and 1j delimits the Central AS region (CAS) that covers most of the winter monsoon bloom. See section 2.3 for reference on the climatological data sets.

related to the outflow of waters from the Gulf of Oman that are not well constrained by the temperature and salinity damping imposed in the model. Similarly to observations, nitrate concentrations in the model are higher in the region of convective mixing (Figures 1g and 1i). We can also note that the mean nitrate concentration in surface waters (0:80 m) is underestimated, particularly in the southwest where MLD are 10 m shallower in the model than in observations (Figures 1b, 1g, and 1i).

[20] The bloom captured by SeaWiFS and simulated by the model during the NEM covers the region of mixing with Chl values typically $\geq$0.2 mg.m$^{-3}$ and a maximum intensity north of 13°N where Chl exceeds 0.5 mg.m$^{-3}$ (Figures 1e and 1j). Chl is however underestimated north of 20°N where values are ~30 – 50% lower than in observations. This bias appears to be a common feature of most modeling studies. It is visible on Figure 6 and 7 in the work by *Kawamiya and Oschlies* [2003]. It is also reported by *Wiggert et al.* [2006] and *Koné et al.* [2009], where it is attributed to the lack of mixed layer diurnal variability, but for different reasons. Whereas *Wiggert et al.* [2006] explain the inconsistencies in the bloom dynamics by an insufficient deepening of the mixed layer and nutrient supply, *Koné et al.* [2009] attribute them to an exaggerated MLD and light limitation. In a sensitivity experiment, we have removed the diurnal heating cycle and this did not significantly modify our model mean state because it did not affect the daily overturning. This suggests that in our model this bias is not linked to the diurnal heating cycle. In fact, the analysis of the phytoplankton nutrient limitations suggests that this bias is partly related to an excessive silicate limitation due to an underestimation of silicate input from the Gulf of Oman. Indeed, despite the underestimation of nitrate concentrations, the diatoms and nanophytoplankton growth are not limited by nitrate. In our model, nitrate and silicate limitation terms are comprised between 0 (maximum limitation) and 1 (no limitation) and depend on the nutrient concentration with respect to the nutrient half-saturation constant (see model formulation in Appendix A). During the NEM, the mean value of these terms is 0.7–0.8 for nitrate and $\leq$0.6 for silicate (Figure 5j). In addition, low surface Chl in the northern AS are also probably related to the bias in MLD that could explain an overestimation of surface chlorophyll dilution (Figures 1b, 1g, and 7) and light limitation (extremely low values of Photosynthetically Available Radiation in Figure 5j).

[21] It is worth noting that the agreement between the model and the observations derived from satellite sensors (SST and Chl) exceeds the one obtained for fields interpolated from *in-situ* measurements at low spatio-temporal resolution (MLD and nitrate concentration). Observations such as the one obtained by the mooring deployed in the northern AS (15.5°N, 61.5°E) that captured MLD varying between 80 and 120 m over a 2 month-period (December to February, *Weller et al.* [2002]) suggest that this lack of resolution could bias these climatologies and explain part of the discrepancy between data and model results.

### 3.2. Southwest Monsoon

[22] During the SWM period, the wind circulation reverses and the strong southwesterly wind jet of warm and moist air (referred to as the Findlater Jet [*Findlater*, 1969]) runs diagonally across the basin with an averaged maximum windstress over the central AS. The main oceanic features associated with these winds are the three coastal upwelling systems that develop along the Omani and Somali coasts and along the southwestern Indian coast. The extent and amplitude of the western upwelling systems are indicated by the presence of SSTs colder than 28°C (Figure 2c).

[23] The upwelling off Somalia is primarily driven by Ekman circulation but is intensified by the circulation in the western boundary current (extensively described by *Schott and McCreary* [2001]). The Somali Current flows northward. It partly crosses the Socotra Passage (passage between Socotra and Somalia) and partly turns offshore forming a series of anticyclonic gyres: the highly energetic Great Whirl near 8°N, the Southern Gyre at the equator and the Socotra Eddy northeast of Socotra (Figure 2a). The upwelling compensates the intense offshore advection associated with the Great Whirl and the Southern Gyre. The Oman upwelling develops in response to the Ekman circulation that dominates the circulation in the northern Arabian Sea [*Schott and McCreary*, 2001]. The upwelling along the southwest coast of India is less intense than the two western boundary upwelling systems. Its development is associated with the propagation of upwelling Kelvin waves and is compensated by the intensification of the WICC that flows southeastward along India [*Shankar and Shetye*, 1997].

[24] The MLD pattern results from the combined effect of strong wind-driven entrainment and lateral variations in Ekman pumping to either side of the Findlater Jet. The entrainment forced over the whole basin by the monsoon winds is modulated by an open ocean upwelling resulting in shallow mixed-layers north of the Findlater Jet and a downwelling associated with much deeper ML to the south (Figure 2b) [*Bauer et al.*, 1991; *Rao et al.*, 1989; *Schott and McCreary*, 2001; *Fischer et al.*, 2002; *Weller et al.*, 2002]. These large-scale circulation, MLD and SST features are very well reproduced by the model (Figures 2a–2c and 2f–2h).

[25] Nitrate is primarily supplied to the surface waters by the three upwelling systems. Concentrations are larger than 4 mmol.m$^{-3}$ along the western boundary coasts and the southwestern Indian coast and decrease toward the central Arabian Sea (Figure 2d). As expected, prominent phytoplankton blooms with Chl concentrations exceeding 2 mg.m$^{-3}$ are apparent in the three upwelling regions: off the coasts of Oman, Somalia and along southwestern India (Figure 2e). The bloom that develops along the western coasts extends offshore into the central AS with Chl values $\geq$0.4 mg.m$^{-3}$ reaching 65°E (Figure 2e).

[26] High Chl values are reproduced by the model in the three upwelling regions. The magnitude and the offshore extent of the bloom in the Somali and Indian upwelling systems are quite well reproduced, with Chl concentrations $\geq$0.4 mg.m$^{-3}$ extending offshore to 62°E and 74°E respectively. The bloom off Oman in underestimated, particularly around 15°N where the offshore extension is reduced by ~300–500 km. Another model bias can be seen around the Great Whirl, where simulated Chl concentrations exceed observations. We believe that these two biases result from the overestimation of the offshore advection by the Great Whirl and an underestimation of the advection through the Socotra Passage, leading to intense outflow of warm and oligotrophic waters from the Gulf of Aden (Figures 2a, 2c,

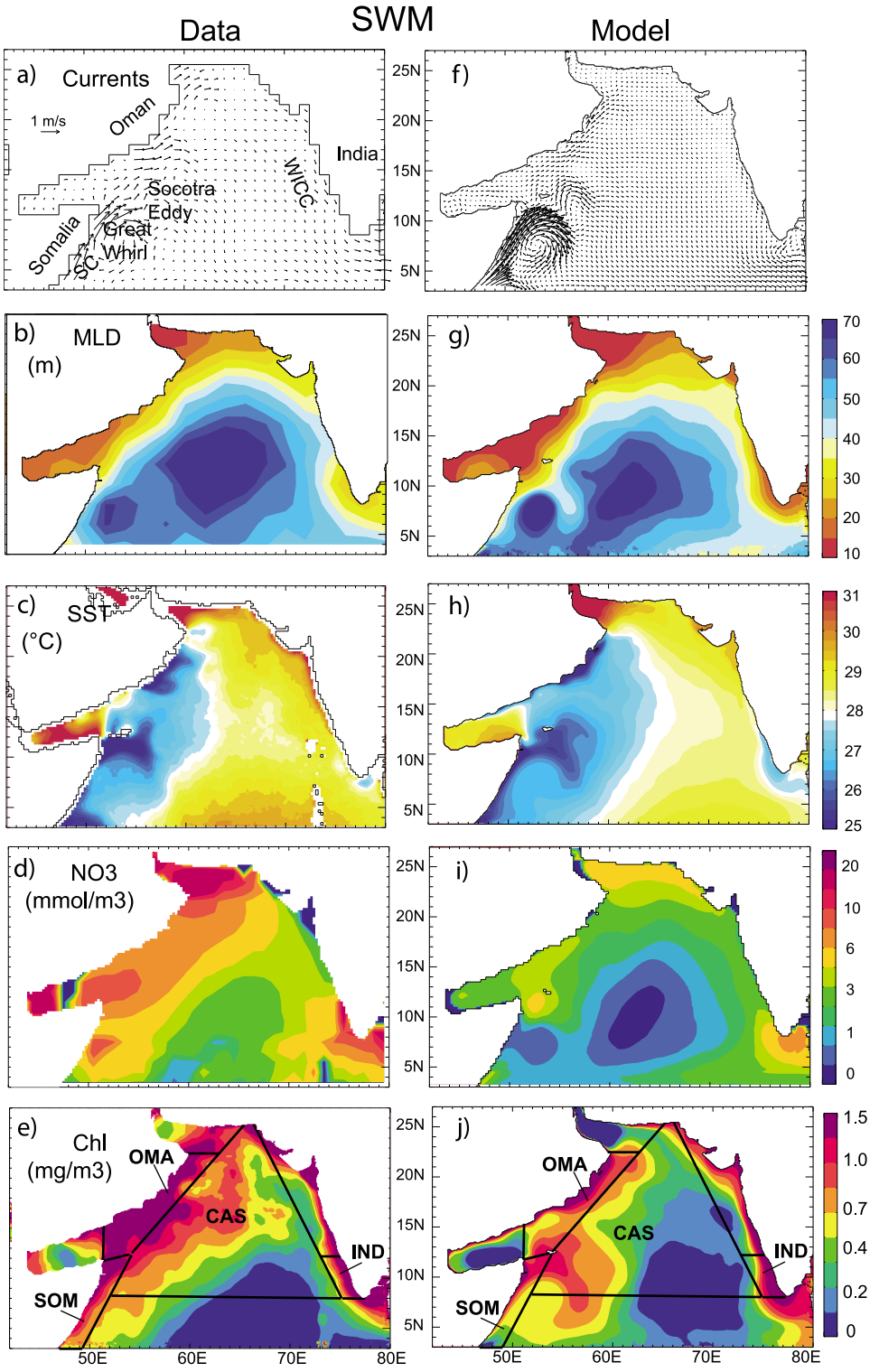


**Figure 2.** Climatological maps of dynamical and biogeochemical properties during the SWM period (Jun-Aug) from (a–e) observations and (f–j) model results. Figures 2a and 2f show currents: SC and WICC refer to the Somali Current and Western Indian Coastal Current respectively. Figures 2b and 2g show mixed-layer depth (MLD, in m) estimated with a temperature threshold of 0.2°C. Figures 2c and 2h show sea surface temperature (SST, in °C). Figures 2d and 2i show nitrate concentration (in mmol. $m^{-3}$) averaged over the upper 80m. Figures 2e and 2j show surface chlorophyll (Chl, in $mg.m^{-3}$). Four blooming regions are delimited: the upwelling systems of Oman (OMA), Somalia (SOM) and southwest India (IND) and the Central AS (CAS). See section 2.3 for reference on the climatological data sets.

2e, 2f, 2h, and 2j). The northward transport through the Socotra Passage during the SWM in the model is indeed only half of the observed estimate of 5 Sv [*Schott and McCreary*, 2001]. We also believe that the marked Chl signature simulated in the Great Whirl region reflects the lack of interannual variability of the Great Whirl position in the model. In the SeaWiFS climatology, the Chl concentration offshore the Somali coast is increased by the presence of the Great Whirl that develops between 5°N and 12.5°N. In the model, the Great Whirl propagates northward until it reaches Socotra, explaining part of the bias in the Chl concentration. The model is also slightly too productive in the band centered around 5°N where the Chl concentration exceeds observed values $\leq$0.2 mg.m$^{-3}$ (Figures 2e and 2j). This bias is attributable to exaggerated input of nutrients by mesoscale vertical velocities, particularly in the region of the Maldive Islands (see nitrate input terms in Figure 9).

### 3.3. Primary Production and Export

[27] To evaluate the model ability in the four blooming regions (defined in Figures 2e and 2j), the range and the mean vertically integrated primary production in the model are compared to observational data (Figure 3). Sites in the central Arabian Sea and along the coasts of Oman and India were sampled in the frame of the US and Indian JGOFS programs between 1994 and 1997 [*Barber et al.*, 2001; *Gauns et al.*, 2005]. Sites in the Somali basin were sampled on board the R.V. *Tyro* in 1992 and published by *Veldhuis et al.* [1997]. Most observations fall in the simulated range and the timing of increased PP associated with the summer and winter blooms are similar (Figure 3). The model however does not reproduce extremely high values observed in the Somali (SOM) upwelling region in early summer and in the central AS (CAS), more particularly in the western CAS at the time of both winter and summer bloom peaks (Figures 3b and 3d).

[28] In a more regional view, the annual vertically integrated PP averaged over the domain in the model (185 gC.m$^{-2}$) is very similar to values estimated from satellite data by *Antoine et al.* [1996] (184 gC.m$^{-2}$) and *Behrenfeld and Falkowski* [1997] (153 gC.m$^{-2}$) and significantly higher than estimates simulated at lower resolution by *Kawamiya and Oschlies* [2003] in their reference run (70 gC.m$^{-2}$) (Table 1). The annual particulate export at 110 m simulated over the region is 28.8 gC.m$^{-2}$, which is in really good agreement with the estimate of ~28.5 gC.m$^{-2}$ derived from JGOFS observations [*Lee et al.*, 1998].

### 3.4. Mesoscale Variability

[29] The mean seasonal pictures described in the previous sections (sections 3.1–3.3) are strongly modulated at the mesoscale. The mesoscale circulation (quantified as the standard deviation of the sea level anomaly std(SLA)) in the Aviso dataset and the model have similar magnitude and distribution, suggesting that mesoscale variability is well captured at 1/12° resolution (Figures 4a and 4c). The mesoscale variability is most intense in the vicinity of the Somali Current and in the Gulf of Aden, where std(SLA) exceeds 5 cm. The highly energetic dynamics associated with the western boundary current is indeed a major generator of mesoscale structures. Besides this region of extremely high variability, the mesoscale circulation is quite intense in the coastal regions offshore Oman and India and in a latitudinal band between 5 and 10°N (std(SLA) between 2 and 3 cm). In coastal regions, baroclinic instabilities enhanced by the presence of upwelling systems during the SWM and the bathymetry promote the formation of mesoscale structures. In the 5–10°N band, the variability is explained by: 1) the meandering of the westward North Equatorial Current [*Kim et al.*, 2001] and 2) the formation of an eddy in the Laccadive Ridge area (72–74°W) that propagates westward as planetary waves [*Shankar and Shetye*, 1997; *Bruce et al.*, 1994]. Finally, the mesoscale variability in the central AS is lower with values of std(SLA) between 1 and 3 cm.

[30] This study presents the first bio-physical model in the AS that explicitly resolves eddies. To assess the gain of resolving the mesoscale, we performed a simulation at eddy-permitting resolution (1/4° horizontal grid resolution), more comparable in terms of resolution to previous bio-physical modeling studies of the region [*Kawamiya*, 2001; *Wiggert et al.*, 2006; *Koné et al.*, 2009]. The mesoscale variability predicted at 1/4° is by far weaker than the at 1/12° (Figures 4b and 4c). At 1/4°, the pattern of extremely high variability (std(SLA) $\leq$ 5 cm) is limited to the northern part of the Great Whirl and the Gulf of Aden; the mesoscale variability in other regions is about twice lower, particularly in the central AS north of 12°N where the std(SLA) hardly exceeds 1.5 cm.

## 4. Blooms and Mesoscale Structure Temporal Evolution

[31] In the previous section we have evaluated the model ability at reproducing the mean seasonal cycle and the mesoscale variability. In this section, we present how the bloom and the mesoscale structures evolve along the seasonal cycle.

[32] In the Arabian Sea, the phytoplankton seasonal cycle is characterized by two minima which occur during the two intermonsoon periods (typically in April and November, Figure 3). These minima delimit two periods which encompass the winter and summer blooms, from the bloom onset until the final bloom decay. More precisely we will refer to these two periods as the winter bloom period (noted WBloom) that extends from December to March (4 month) and summer bloom period (noted SBloom) that extends from April to November (4 month). This definition allows us to describe the dynamical and biogeochemical forcing of the blooms associated with both monsoons, even though it has been previously acknowledged that the exact timing of the two bloom periods varies spatially over the AS [*Lévy et al.*, 2007].

### 4.1. Winter Bloom and Mesoscale Eddies

[33] The regions defined as central Arabian Sea (CAS), Somali (SOM) and Omani (OMA) (defined in Figures 1, 2e, and 2j) capture a bloom during the WBloom period (Figures 5b, 5e, and 5k). However, in the present study, the winter bloom will be discussed focusing on the CAS region in order to clearly distinguish the processes of the winter bloom from the one associated with the upwelling regions. The CAS bloom in the model is triggered in December when the ML deepens and reaches ~50 m, bringing nutrients

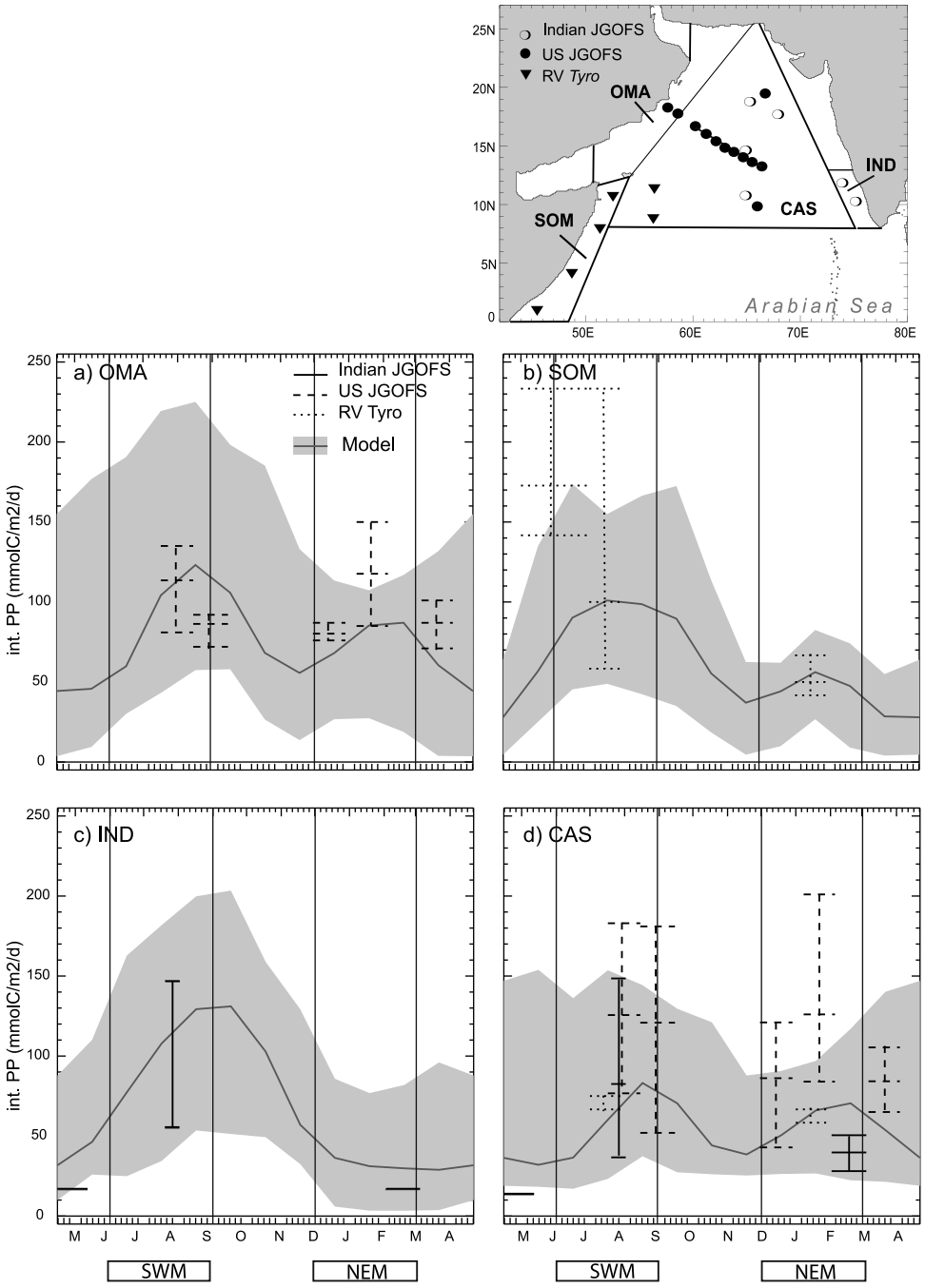


**Figure 3.** Vertically integrated primary production (PP, in mmol $C.m^{-2}.d^{-1}$) in the (a) OMA, (b) SOM, (c) IND, and (d) CAS regions: the model mean (grey line) and spatial range (grey shading, minimum-maximum values) over the region are compared to the mean and range of primary estimated from Indian JGOFS stations (2 in IND and 4 in CAS), US JGOFS stations (S2-S3 in OMA, N7 and S4 to S11 in CAS) and on board the RV *Tyro* (4 in SOM and 2 in CAS). The map indicates the position of the stations.

and lowering the nitrogen limitation in the surface layer (Figures 5j–5l). During that period, deep ML lower the mean photosynthetically available radiation (PAR), slightly limiting phytoplankton growth (Figure 5j). The phytoplankton biomass peaks in late February when the ML restratifies with an averaged concentration of ~1.8 $mmolC.m^{-3}$ for the CAS region. The phytoplankton assemblage predicted by the model is dominated by small-size phytoplankton, while diatoms account for ~15 – 25% of the total phytoplankton biomass (Figure 5k). The low contribution of diatoms is explained by the strong silicate limitation (≤0.6) during the whole Wbloom period (Figure 5j).

[34] This climatological evolution of the bloom is however modulated spatially by the presence of mesoscale structures. A general feature of the model and the few *in-situ* [*Marra and Barber*, 2005] and satellite observations is that surface Chl concentrations are significantly larger inside some eddies (E1) or in elongated filaments of ~30 km width

**Table 1.** Annual Integrated PP Over the Arabian Sea in Model Simulations[a]

| Estimates | Method | PP ($gC.m^{-2}$) |
|---|---|---|
| This study | biophysical model 1/12° | 185 |
| *Kawamiya and Oschlies* [2003] | biophysical model 1/3° | 70 |
| *Behrenfeld and Falkowski* [1997] | Chl satellite-based | 153 |
| *Antoine et al.* [1996] | Chl satellite-based | 184 |

[a]Area for this study: 40°E–80°E and 5°S–27°N and for others: 8°S–27°N.

wrapped around eddies (F1 and F2) (see Figures 6a, 6b, 6e, and 6f). Most of these structures of high surface Chl concentrations are associated with shallow ML in the model (Figure 7). The systematic association of high surface Chl concentrations with shallow MLDs rises the question of whether the surface signature reflects the lack of Chl dilution or the integrated phytoplanktonic concentrations in the water column. High surface Chl concentrations are not generally associated with high integrated Chl (F2). In such cases high surface Chl concentrations in mesoscale structures reflect the low dilution associated with shallow ML (Figure 7). However, in other cases high surface Chl and integrated Chl coincide, suggesting that mesoscale structures could influence the phytoplankton growth (F1).

[35] In the model, these mesoscale structures are also associated with relatively large vertical velocities (5 days $|w| \geq 5$ $m.d^{-1}$, Figure 7), which could impact the nutrient budget in the region even if the regional mean vertical velocity is weak (Figure 5l). The vertically increasing concentration of nutrients such as nitrate makes the impact of upward and downward vertical velocities on the nutrient supply very different: upward velocities transport nutrients to the upper layer where they can be consumed by the phytoplankton, whereas downward velocities transport nutrient-poor waters to deeper layers. This possible impact of vertical velocities associated with mesoscale dynamics will be discussed in section 5.

### 4.2. Summer Blooms and Filamentary Structures

[36] In the three upwelling regions of OMA, SOM and India (IND), the bloom is sustained by the vertical advection of nutrients (Figure 2d) [*Banse*, 1987; *Marra and Barber*, 2005; *Lévy et al.*, 2007]. In the model, the three blooms start about one month after the upwelling started (positive vertical velocity: $W \geq 0$ in Figure 5). The phytoplankton peaks with values of 2–2.5 $mmolC.m^{-3}$ in the three upwelling systems (Figures 5b, 5e, and 5h) but with different upwelling strength and blooming period (Figures 5c, 5f, and 5i). The upwelling starts in early-SBloom in SOM and IND, triggering blooms that last 6 month (May-Oct in SOM and June-November in IND), while it onsets in mid-SBloom and lasts 4 month (July-October) in OMA. In the CAS, the summer bloom is short-lived and weaker than in upwelling regions: it onsets in June-July and peaks in August with phytoplankton concentrations that are $\leq 2$ $mmolC.m^{-3}$ (Figure 5k). Consistently with *in-situ* observations that show a decrease of diatoms proportion from upwelling areas to offshore regions [*Banse*, 1994; *Garrison et al.*, 1998; *Toon et al.*, 2000], diatoms account for 20 to 40% of the phytoplankton assemblage in SOM, OMA and IND, while they represent 15 to 20% of the biomass in CAS (Figures 5b, 5e, 5h, and 5k).

[37] The highest Chl concentrations in satellite observations and in the model are found along the three upwelling systems ($\geq 2$ $mg.m^{-3}$) as well as in mesoscale filaments that extend offshore (F3-F5 in Figures 6c, 6d, 6g, and 6h). These filamentary structures are the largest offshore of the western boundary upwelling systems, where they reach ~100 km width and ~500–1000 km long (Figure 6). Offshore Somalia, the bloom in the model starts in three major filaments: two of them are wrapped around the Great Whirl and the Southern Gyre, whereas the third one enters the Socotra Passage (Figures 6c and 6g). Later during the SBloom period, the bloom is reduced in the south and propagates to the Socotra Eddy (Figures 6d and 6h). This evolution of the bloom is consistent with the description of the circulation in the region. Upwelled waters are primarily advected through the Southern Gyre, the Great Whirl and the Socotra Passage [*Schott and McCreary*, 2001]. Toward the end of the SBloom period, the Southern Gyre collapses, the flow through the Socotra Passage decreases and the main pathway of advection shifts to the Great Whirl and the Socotra Eddy [*Schott and McCreary*, 2001; *Schott et al.*, 1997].

[38] During the early-SBloom, the extension of filaments offshore the Omani coast is weaker than offshore Somalia (Figure 6g). This difference between the two western

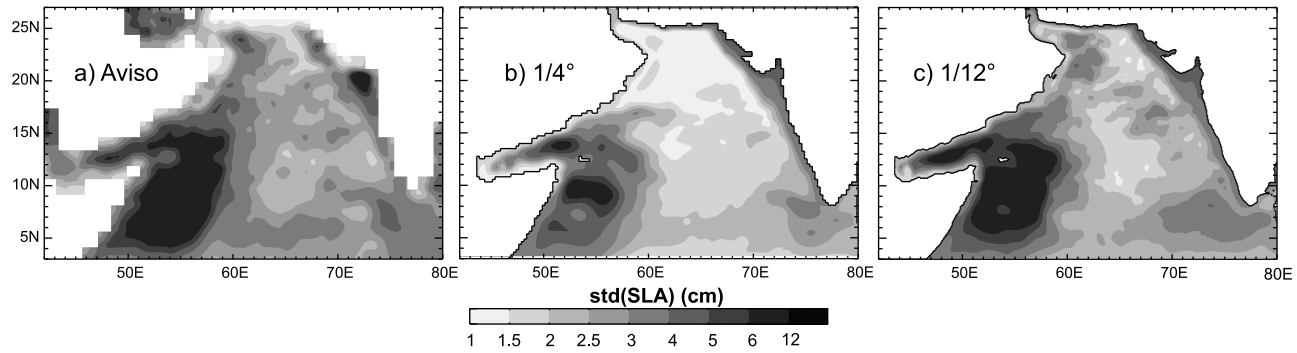


**Figure 4.** (a) Mesoscale circulation estimated from the AVISO dataset and in the model at (b) eddy-permitting resolution and (c) eddy-resolving resolution. The mesoscale circulation is quantified by the standard deviation of the sea level anomaly (SLA) filtered in the 14–120 days band, over the 1995–2003 period.

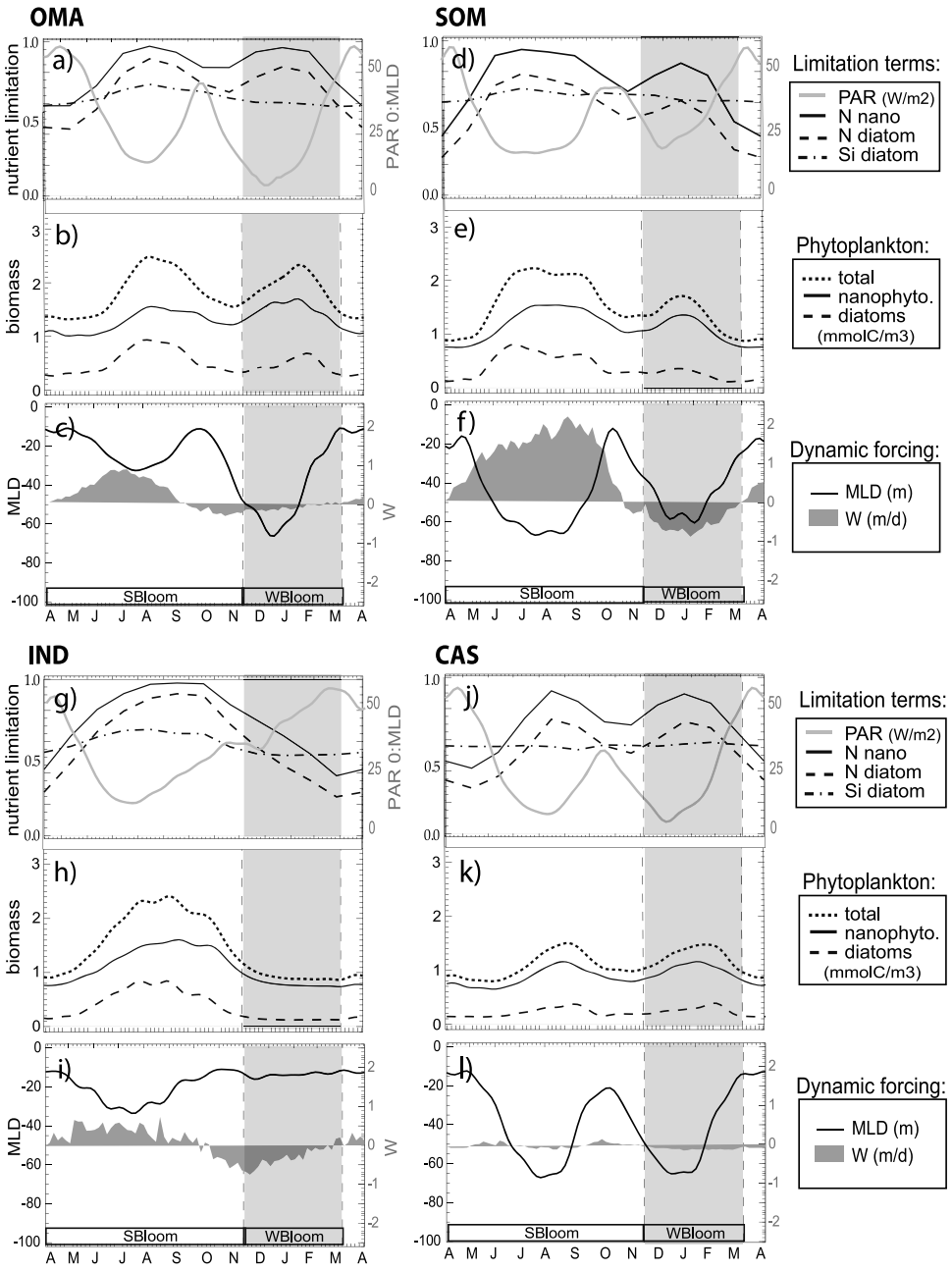


**Figure 5.** Mean climatological time series of limitation terms, phytoplankton and dynamic forcing over the (a–c) OMA, (d–f) SOM, (g–i) IND, and (j–l) CAS regions (delimited in Figures 1 and 2). In Figures 5a, 5d, 5g, and 5j, growth limitation terms are averaged over the upper 80 m: the solid line shows the nanophytoplankton nitrogen limitation and the dashed lines show the diatom limitation by nitrogen and silicate. The grey line indicates the photosynthetically available radiation (PAR) averaged over the MLD (in $W.m^{-2}$). In Figures 5b, 5e, 5h, and 5k, phytoplankton biomass is averaged over the upper 80 m (in $mmolC.m^{-3}$): the dotted line shows the total biomass (nanophytoplankton + diatom); nanophytoplankton and diatom biomass are indicated by the solid and dashed lines respectively. Figures 5c, 5f, 5i, and 5l show MLD (in m) and vertical velocities at 80 m (W in $m.d^{-1}$).

boundary upwelling is attributable to the delay in the upwelling onset (Figures 5c and 5f) and the lower horizontal velocities of mesoscale structures in the upwelling of Oman (Figure 2f). Three filaments develop in the model: one offshore Haswayn (F3) and two between Ras Shirbthat and Ras Al Hadd (F4 and F5). Toward the end of the SBloom period, the filament F3 as merged with the Socotra Eddy and the two northern filaments extend into the AS as far as 65°E in both observations and model results (F4′-F4, F5′-F5 in Figures 6 and 7).

[39] The bloom extension offshore the Indian upwelling is much weaker than offshore Oman and Somalia, where

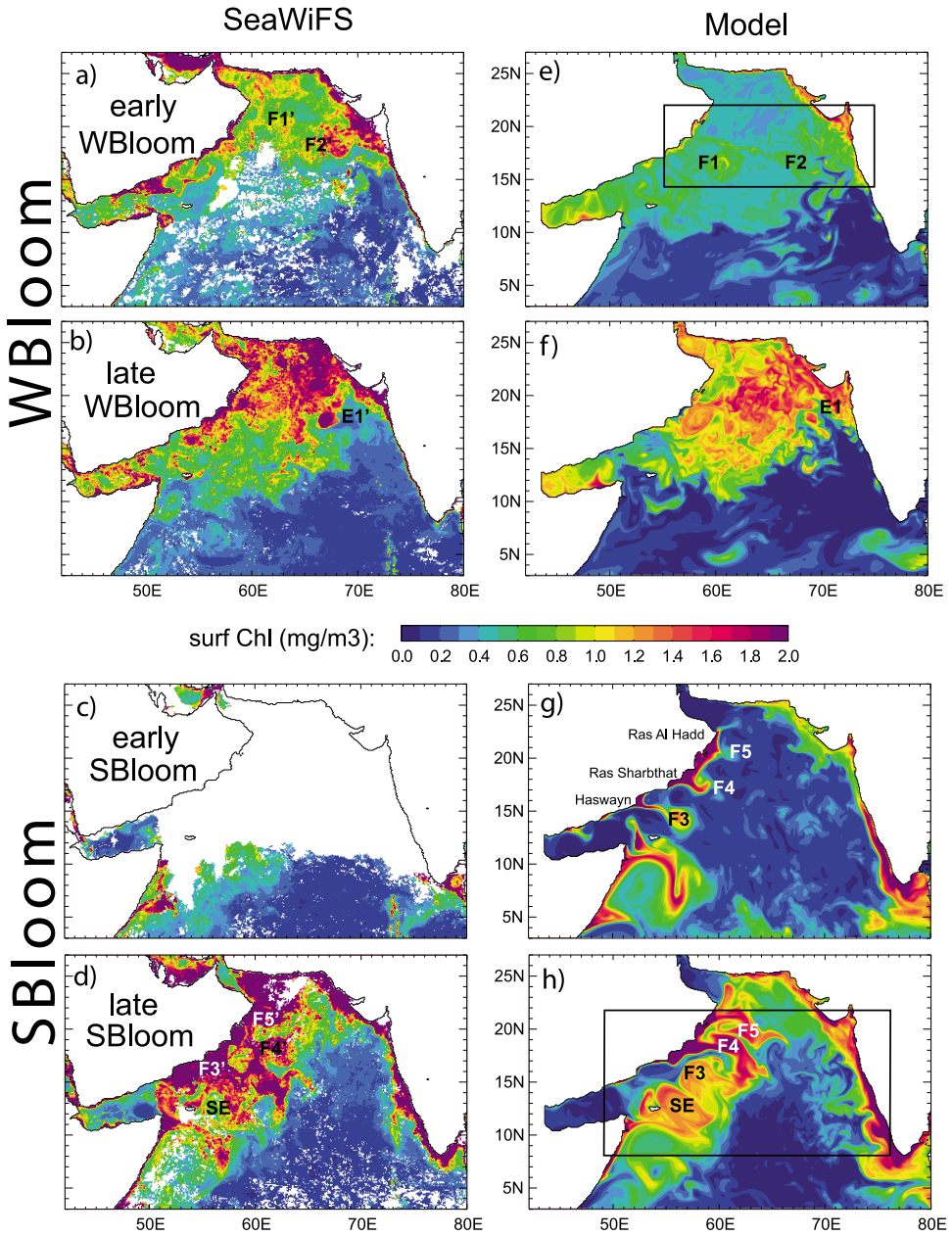


**Figure 6.** Surface chlorophyll snapshots in (a and e) early WBloom (Jan. 25, 2002), (b and f) late WBloom (March. 1, 2002), (c and g) early SBloom (June. 26, 2002), and (d and h) late SBloom (Sept. 15, 2002). Observations are 8 days composite SeaWiFS images (Figures 6a–6d) and model results are averaged over 5 days (Figures 6e–6h). Black rectangles indicate zooms of Figures 7a–7d and 7e–7h.

strong upwelling and energetic mesoscale structures associated with the western boundary current reinforce the advection of upwelled waters. High Chl concentrations upwelled waters ($\geq$1.5 mg.m$^{-3}$) are advected offshore inside eddy cores and through small filaments of ~10–50 km width that develop along Indian the coast during the summer (Figure 6).

[40] In the model, there is a strong contrast in mesoscale vertical velocities between the Somali region and the two other upwelling systems: vertical velocities in filaments wrapped around the Southern Gyre, the Great Whirl and the Socotra Eddy are intense ($|w| \geq 5$ m.d$^{-1}$), while they remain relatively weak in structures offshore Oman (F3, F4, F5) and India ($|w| \leq 5$ m.d$^{-1}$, Figure 7). Contrasting with the situation during the WBloom period, surface and integrated Chl distributions are similar suggesting that the surface signature is a good proxy in indicating the presence of higher integrated phytoplanktonic concentrations. However, it is worth noting that anomalously low surface Chl concentrations simulated by the model north of Socotra Island are associated with relatively high integrated concentrations (Figure 7). We attribute this difference to the outflow of warm and oligotrophic waters from the Aden Gulf that overlap colder and

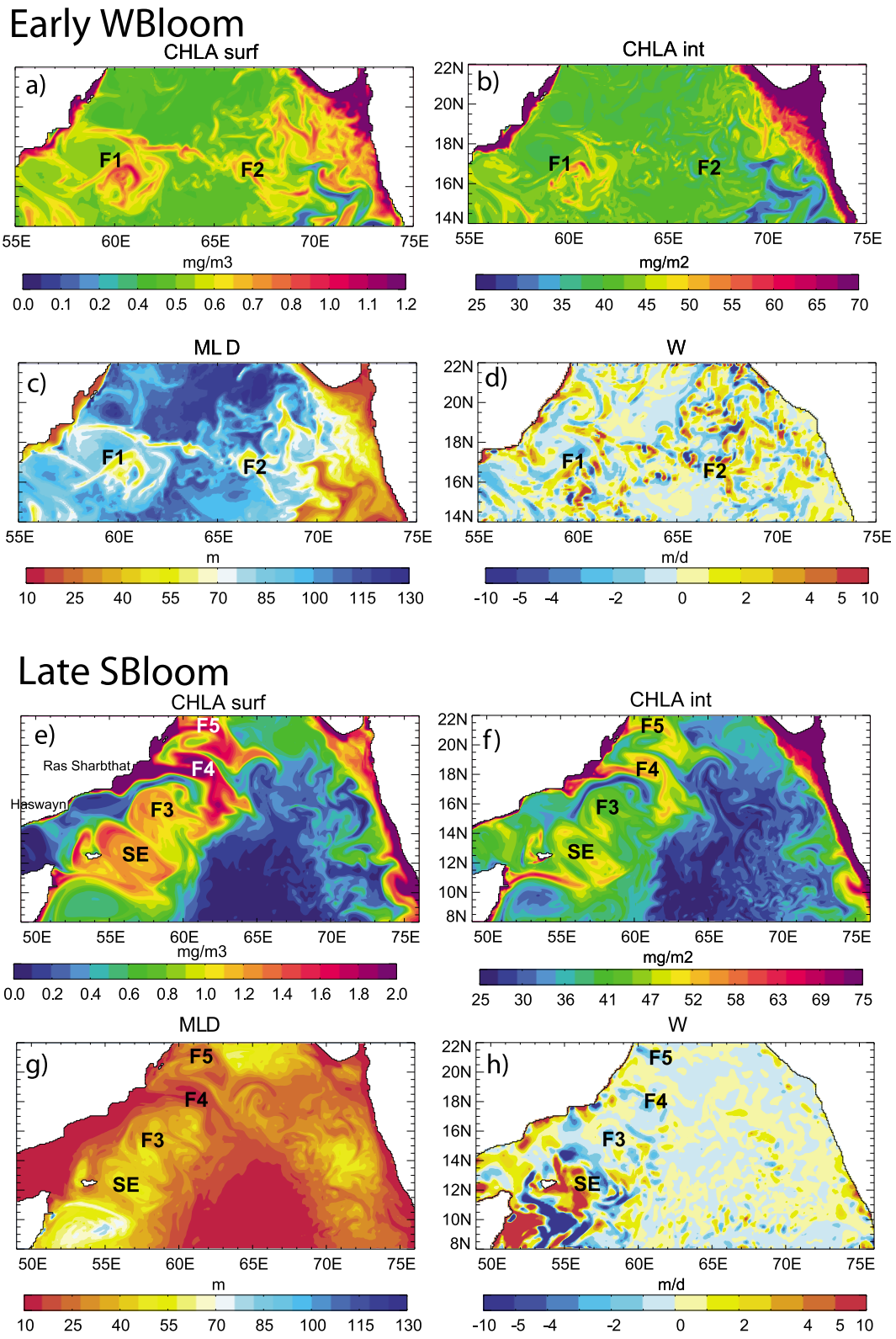


**Figure 7.** Model 5 days average snapshots in (a–d) early WBloom (Jan. 25, 2002) and (e–h) late SBloom (Sept. 15, 2002) over the area marked in Figures 6e and 6h: Figures 7a and 7e show surface Chl, Figures 7b and 7f show integrated Chl (0:80 m), Figures 7c and 7g show MLD, and Figures 7d and 7h show vertical velocities at 80 m.

more productive waters originated from western boundary upwelling systems.

## 5. Mesoscale Influence on Nutrient Budget

[41] The previous section showed the strong imprints of the mesoscale circulation on the instantaneous chlorophyll distribution and dynamical fields such as MLD and vertical velocities. In this section, we further examine the influence of mesoscale dynamics on biological production by quantifying its impact on the nutrient budget.

[42] The supply of a nutrient N to the upper layer (defined here as 80m) is by lateral advection ($-u_H.\nabla_H N$), vertical advection ($-u_Z.\nabla_Z N$) and vertical mixing ($\frac{\partial K_z \partial N}{\partial z^2}$). Following the Reynolds averaging method, the lateral and vertical advective supply of N can be separated into contributions from the mean flow and from the fluctuating "eddy" flow:

$$\underbrace{\int_{z=80m}^{0}\left(\overline{-u_H.\nabla_H N}\right)dz}_{\text{total lateral advection}} = \underbrace{\int_{z=80m}^{0}\left(\overline{-u_H}\,.\overline{\nabla_H N}\right)dz}_{\text{mean lateral flow}} + \underbrace{\int_{z=80m}^{0}\left(\overline{-u_H'.\nabla_H N'}\right)dz}_{\text{eddy lateral flow}} \quad (1)$$

$$\underbrace{\int_{z=80m}^{0}\left(\overline{-w.\nabla_Z N}\right)dz}_{\text{total vertical advection}} = \underbrace{\int_{z=80m}^{0}\left(\overline{-w}\,.\overline{\nabla_Z N}\right)dz}_{\text{mean vertical flow}} + \underbrace{\int_{z=80m}^{0}\left(\overline{-w'.\nabla_Z N'}\right)dz}_{\text{eddy vertical flow}} \quad (2)$$

where the over-bar denotes a time mean to be defined and the prime all deviations from this time mean (referred as the eddy term). To exclude the contribution of seasonal variations from the eddy term and incorporate them into the mean term, we defined the mean state of $\overline{u_H}$, $\overline{w}$ and $\overline{N}$ as the monthly, ten-year mean climatology of $u_H$, $w$ and $N$.

[43] In the model, nitrogen is the only nutrient limiting the growth of nanophytoplankton, while diatom growth is limited by nitrate ($NO_3$) at the beginning of the blooms and then by silicate (Si) (Figure 5). The different terms in equations (1) and (2) were evaluated for $N = NO_3$ and $N =$ Si. Transport patterns for the two nutrients are very similar. This is not surprising because N and Si are subjected to the same dynamic and their reservoir location are comparable except north of 20°N where Si concentrations in the model are particularly low. We therefore focus the rest of the analysis on the nitrate budget. As transport terms compensate both spatially and temporally, the spatial structure is presented in Figures 8 and 9, whereas the temporal evolution in the four blooming regions is shown in Figure 10. A summary of nitrate and silicate results will be presented in section 6 and Table 2.

[44] The importance of the eddy transport is quantified by the ratio of the eddy advection over the absolute mean advection $\frac{\text{eddy H + eddy Z}}{|\text{mean H + mean Z}|}$ (Figures 8i and 9i). Values between −1 and 1 (in white) indicate where the mean advection is the main contributor to the nutrient advection, while colored areas highlight where the eddy-induced advection is the main source of nutrient (values >1 indicate an input and values <−1 an output of nitrate from the surface layer).

### 5.1. Eddy-Induced Vertical Advection During Winter

[45] The major source of nutrient to the CAS in the model is convective mixing (Figure 8b). However, nutrients are also supplied to the northern CAS by advection (Figures 8a and 10g). In most of the CAS, the advective transport is dominated by the eddy flow, which is 50 to 100% larger than the mean flow and in particular by the vertical component of the eddy flow that brings ~40% of the nitrate to the upper layer (Figures 8c, 8d, 8i, and 10h). The convective input of nutrients triggered in November-December is thus completed by the eddy-induced vertical advection that is most intense in January and February (Figures 10g and 10h). The vertical velocities associated with mesoscale structures evidenced by model snapshots during the WBloom period (Figure 7) influence the regional and seasonal nutrient budget by promoting the input of nutrients and therefore the phytoplankton growth in the CAS.

### 5.2. Eddy Lateral Advection From Upwelling Systems During Summer

[46] During the SBloom period, our analysis reveals a sharp contrast between upwelling systems where the mean flow dominates the nutrient transport and the CAS where the eddy flow can be 2 to 3 times higher than the mean flow (Figure 9i). More precisely, nutrients are primarily supplied to the upper layer by vertical advection in the upwelling systems of SOM, OMA and IND and then redistributed in the CAS by lateral advection (Figures 9a, 9e, and 9g). Although over the season nutrient transport is on average dominated by the mean flow in upwelling systems, the contribution of the eddy flow plays a significant role that evolves from the supply of nutrients in the early-SBloom period to the export of nutrients toward the end of the SBloom period (Figures 10a–10f).

[47] During the early SBloom period, the bloom in upwelling regions is sustained by the eddy-induced vertical advection, whereas the contribution of mean vertical advection is negligible (Figures 10a–10f). Later in the season, the mean flow (vertical + horizontal) supplies most of the nutrients that are then exported by the eddy lateral advection. It is interesting to note that in upwelling systems the input of nutrients by mean vertical and mean lateral advections are of the same order of magnitude. In our model, this large contribution of the mean lateral advection is attributed to the SWM circulation that transports nutrients from the upwelling zone south of SOM (Southern Gyre region) northward through SOM and the Socotra Passage and then into OMA. Along the western coast of India, nutrients originated from the northeastern AS and from river input are advected southward by the WICC into IND (Figure 9).

[48] Although some similarities arise between the three upwelling systems, the intense circulation in SOM leads to a substantially different response in the eddy transport. In SOM the eddy vertical input and eddy lateral export of nutrients take place over the whole SBloom period (Figure 10d). In OMA and IND, the eddy vertical advection supplies nutrients only during early-SBloom and the eddy lateral advection exports nutrients only during late-SBloom. This contrast in eddy

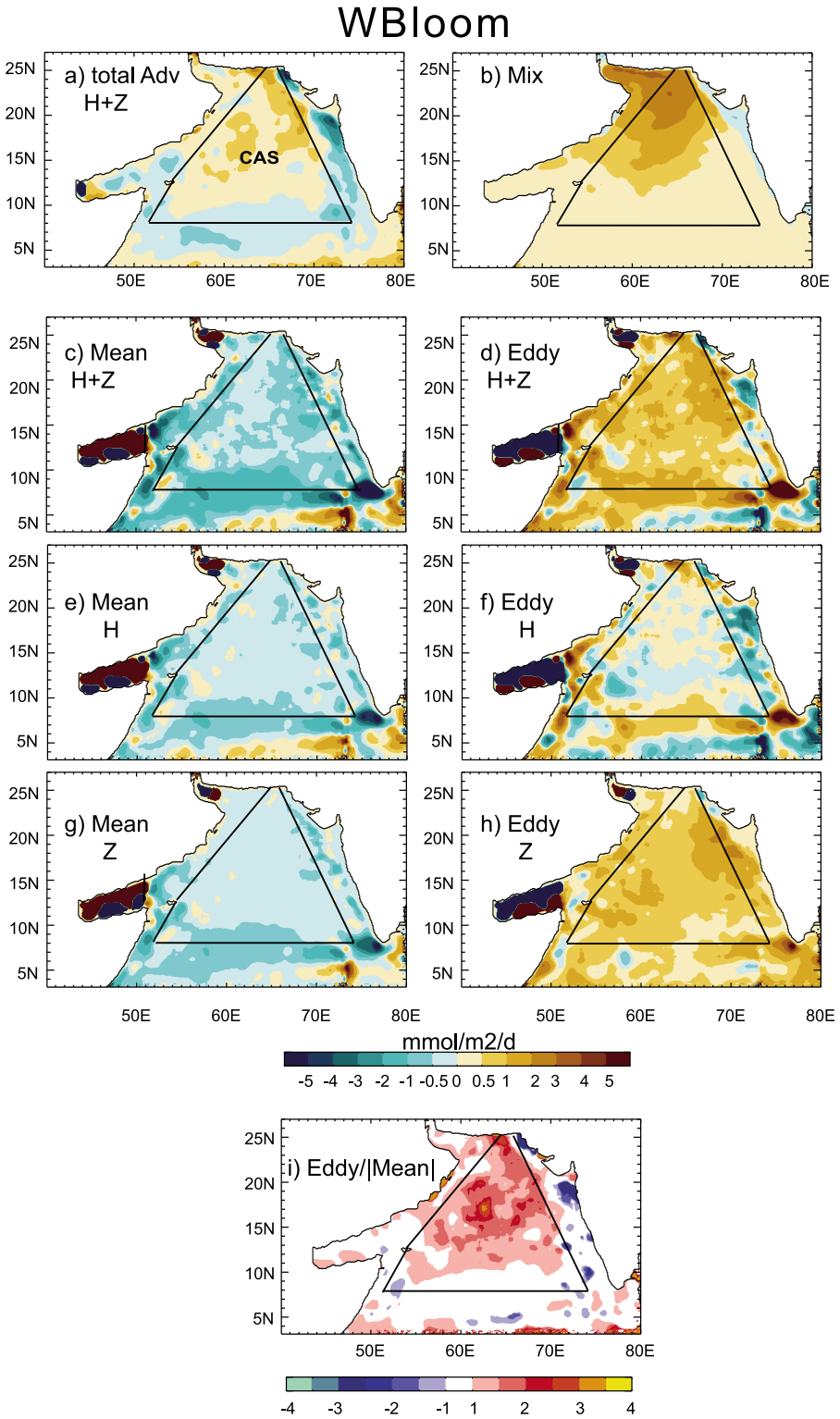


**Figure 8.** Climatological maps of nitrate trends simulated in the upper 80 m during the WBloom period (in mmol.m$^{-2}$.d$^{-1}$): (a) total advective trend (horizontal + vertical); (b) mixing trend; (c, e, and g) mean flow contribution to total advection, horizontal advection and vertical advection; (d, f, and h) eddy flow contribution to total advection, horizontal advection and vertical advection; and (i) eddy contribution compared to the absolute mean contribution. Colors indicate where the eddy flow contribution to nitrate trend is larger than the mean flow contribution (values ≥1 (≤−1) indicate an input (output) of nitrate from the surface layer).

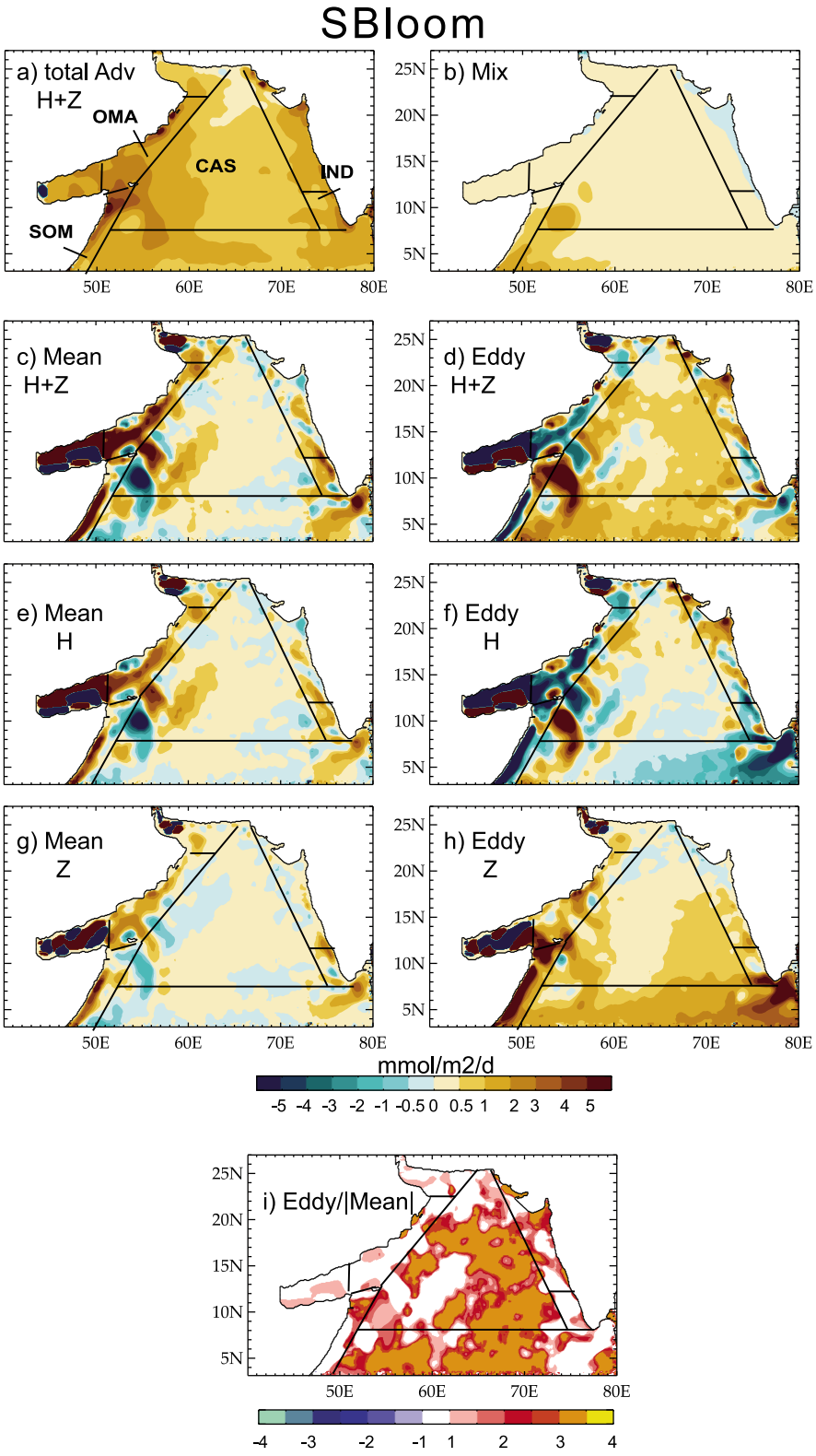


**Figure 9.** Climatological maps of nitrate trends simulated in the upper 80 m during the SBloom period (in $mmol.m^{-2}.d^{-1}$): (a) total advective trend (horizontal + vertical); (b) mixing trend; (c, e, and g) mean flow contribution to total advection, horizontal advection and vertical advection; (d, f, and h) eddy flow contribution to total advection, horizontal advection and vertical advection; and (i) eddy contribution compared to the absolute mean contribution. Colors indicate where the eddy flow contribution to nitrate trend is larger than the mean flow contribution (values $\geq 1$ ($\leq -1$) indicate an input (output) of nitrate from the surface layer).

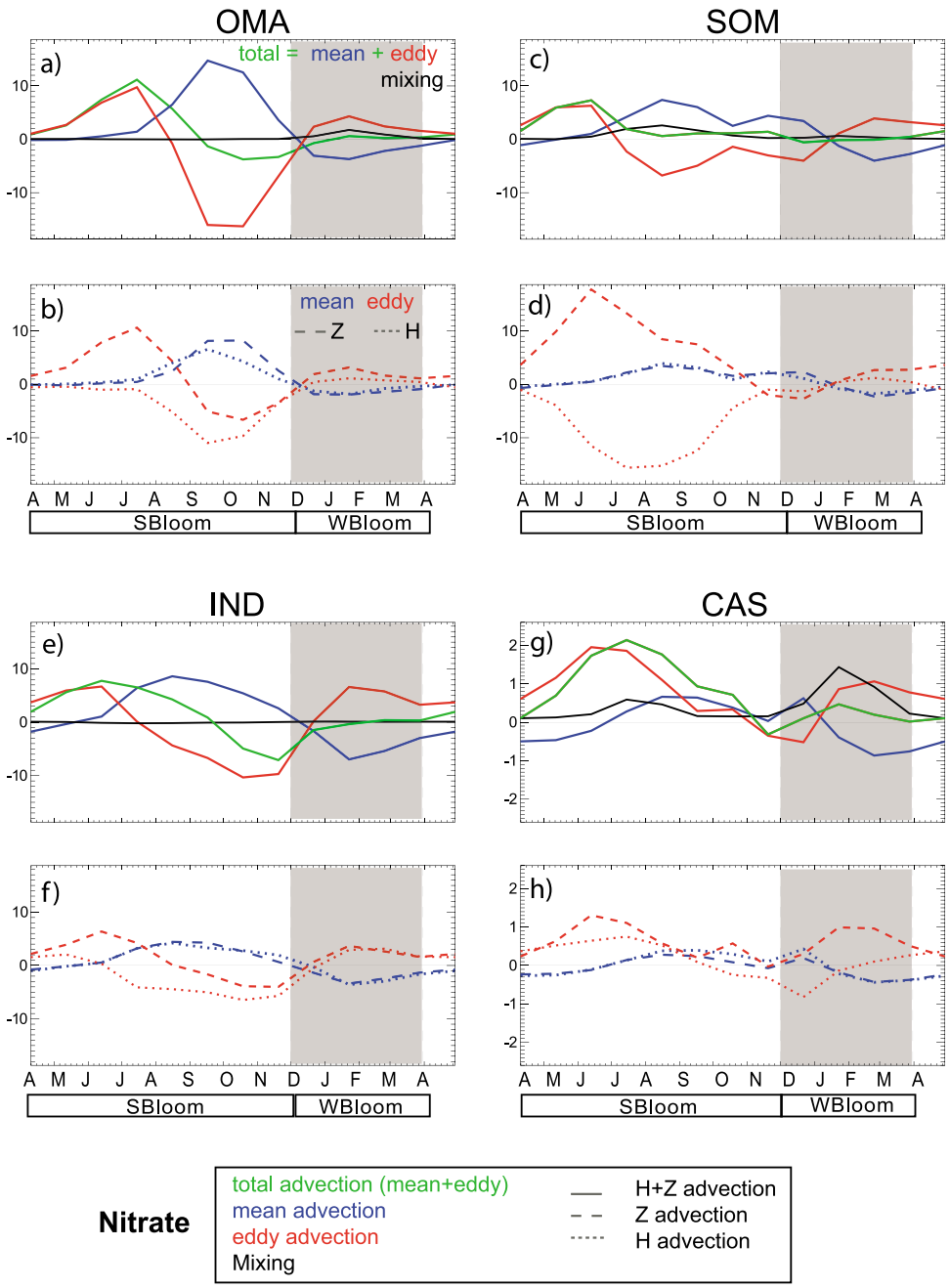


**Figure 10.** Climatological time series of nitrate trends simulated in R12 averaged over the upper 80m in (a and b) OMA, (c and d) SOM, (e and f) IND, and (g and h) CAS. Figures 10a, 10c, 10e, and 10g show the vertical mixing (black), the mean advection (blue), the eddy advection (red) and the total advection (green). Figures 10b, 10d, 10f, and 10h partition the mean and eddy advection shown in Figures 10a, 10c, 10e, and 10g into the horizontal (dotted) and vertical (dashed) components.

transport intensity can be attributed to the strong horizontal and vertical velocities associated with mesoscale structures formed in the western boundary current off Somalia.

### 5.3. Lateral and Vertical Eddy Advection in CAS During Summer

[49] The supply of nutrients into CAS displays a east/west contrast. In the western CAS, nutrients are supplied both by the mean and eddy flow lateral advection, whereas in the eastern CAS the eddy flow is the major source of nutrients (Figures 9c, 9d, and 9i). In early-SBloom, nutrients are entirely supplied by the eddy-induced vertical and lateral advection (Figures 10g and 10h). The eddy vertical input is mostly located in the eastern CAS. In contrast, the eddy lateral input mostly takes place in the south-western CAS and corresponds to an export out of SOM, which is the only upwelling region exporting nutrient laterally during that period (Figures 9h, 10g, and 10h).

[50] Toward the end of the SBloom period, the contribution of eddy-induced advection decreases to values of

**Table 2.** Nitrate and Silicate Transport Budgets During the WBloom (December-March), Early SBloom (April-July), and Late SBloom (August-November) Periods Over the Regions OMA, SOM, IND, and CAS[a]

| Nutrient | Region | Period | Mixing | Mean Advection | Eddy Advection | Total |
|---|---|---|---|---|---|---|
| $NO_3$ | OMA | early SBloom | <0.1 | 0.45 | 5.1 | 5.58 |
| $NO_3$ | OMA | late SBloom | <0.1 | 9.36 | −10.0 | −0.64 |
| $NO_3$ | SOM | early SBloom | 0.65 | 1.01 | 3.16 | 4.81 |
| $NO_3$ | SOM | late SBloom | 1.31 | 5.09 | −4.03 | 2.38 |
| $NO_3$ | IND | early SBloom | <0.1 | 1.34 | 4.12 | 5.43 |
| $NO_3$ | IND | late SBloom | <0.1 | 6.06 | −7.77 | −1.77 |
| $NO_3$ | CAS | SBloom | 0.24 | 0.1 | 0.87 | 1.21 |
| $NO_3$ | CAS | WBloom | 0.76 | −0.35 | 0.54 | 0.96 |
| Si | OMA | early SBloom | <0.1 | 0.15 | 2.92 | 3.05 |
| Si | OMA | late SBloom | <0.1 | 6.04 | −6.0 | <0.1 |
| Si | SOM | early SBloom | 0.5 | 0.6 | −2.03 | 3.13 |
| Si | SOM | late SBloom | 1.09 | 5.22 | −5.27 | 1.05 |
| Si | IND | early SBloom | −0.12 | 0.94 | 2.74 | 3.55 |
| Si | IND | late SBloom | −0.25 | 4.2 | −4.8 | −0.85 |
| Si | CAS | SBloom | 0.12 | 0.15 | 0.3 | 0.57 |
| Si | CAS | WBloom | 0.33 | −0.1 | 0.32 | 0.54 |

[a]Results are integrated over the upper 80 m. Units are mmol.m$^{-2}$.d$^{-1}$.

the same order of magnitude than the mean advection (Figure 5g). The mean flow exports nutrient-rich waters upwelled in SOM northward through the Socotra Passage into OMA and eastward through the Great Whirl and Socotra Eddy, which finally fuels the CAS (Figure 9e).

[51] The eddy flow augments the input of nutrients in the western CAS mainly through four pathways. Three filament that develop offshore Haswayn, Ras Sharbthat and Ras Al Hadd in early-SBloom (Figure 6g). The southern filament supply nutrients by both lateral and vertical advection and merge with the Socotra Eddy toward the end of the end of the SBloom period (Figures 9f, 9h, and 6h). The two northern filaments extend offshore throughout the SBloom period and laterally export nutrients in the northern CAS. The difference in vertical advection between the southern and northern filaments in the model is attributed to the proximity of the energetic Socotra Eddy that promotes vertical velocities (Figure 7).

## 6. Discussion

### 6.1. Vertical Processes During Winter: Dilution and Mesoscale Transport

[52] During the winter bloom, phytoplankton concentration increases as the MLD deepens, which is consistent with previous studies [*Banse*, 1987; *Madhupratap et al.*, 1996; *Banse and English*, 2000; *Barber et al.*, 2001; *Prasanna Kumar et al.*, 2001]. Two hypothesis were formulated in

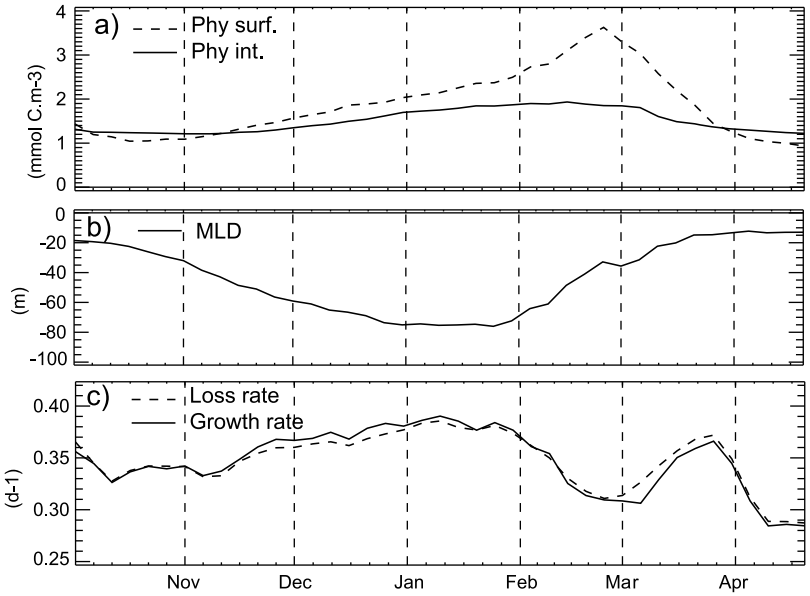


**Figure 11.** Climatological time series in the CAS region: (a) phytoplankton concentration at the surface (dashed) and averaged between the surface and 80 m (solid), (b) MLD, and (c) integrated rates of phytoplankton source (solid) and sinks (dashed). Rates are computed as $\frac{1}{80m}\int_{z=80m}^{0}\frac{X}{PHY}$, where $X$ stands for the different source (primary production) and sink (grazing and mortality) terms. See Appendix A for source and sink formulation.

the literature to explain the phytoplankton response to the ML deepening: 1) the nutrient limitation is lowered by the entrainment of nutrients thus favoring phytoplankton production [*Banse and McClain*, 1986; *Madhupratap et al.*, 1996; *Wiggert et al.*, 2000; *Prasanna Kumar and Narvekar*, 2005] and 2) the ML deepening that dilutes all planktonic groups does not exceed the euphotic depth thus lowering the grazing pressure without limiting the phytoplankton growth [*Marra and Barber*, 2005; *Behrenfeld*, 2010]. In our model, it appears that both the integrated phytoplankton growth (primary production) and loss (grazing + mortality, grazing contributing to 50–70% of the total loss) rates increase while the ML deepens (Figure 11c), supporting the first hypothesis but also that the light limitation is of secondary importance.

[53] Another striking result is the decoupling between the surface and integrated phytoplankton concentrations (Figure 11a). When the ML deepens (Nov-Jan), the surface concentration starts increasing while being diluted (in response to nutrient enrichment). In February, when the restratification occurs and the dilution ends, the surface concentration drastically increases in response to a lower light limitation in the mixed-layer. At the same time, the integrated biomass starts to decrease (loss rate exceeds growth rate, Figure 11c) in response to a decrease of nutrient input by mixing and advection (Figure 10g), which increases the nutrient limitation (Figure 5j).

[54] These climatological mechanisms regulating the winter bloom are modulated by the mesoscale dynamics. Our model reproduces the amplitude of mesoscale variability and the numerous eddies expected from satellite and *in-situ* observations (sections 3.4 and 4 and Figures 4 and 6). Most of these structures are associated with high surface Chl concentrations in both SeaWiFS and the model results. The introduced spatial variability is ~1 $mg.m^{-3}$ over 50–100 km, which is in agreement with the variability associated with an eddy observed during the US JGOFS program [*Marra and Barber*, 2005, Figure 1a] and of the same order as the seasonal variability in the central AS (Figures 6b and 6f). However, our results suggest that the strong surface Chl gradients shaped by winter mesoscale structures are not systematically an indicator of the integrated biomass but highlight the spatial variability in Chl dilution. Mesoscale filaments are associated with shallow ML depth (~50 m) compared to the surrounding values (~100–120m, Figure 7). This restratification effect of the mesoscale is related to the presence of density fronts that become unstable as the eddy field is stirred and deformed [*Lapeyre et al.*, 2006; *Lévy et al.*, 2010]. The stabilization of these fronts generates an ageostrophic circulation, which tends to restratify the water column, as shown in previous eddy-resolving model studies in the North Atlantic [*Nurser and Zhang*, 2000; *Oschlies*, 2002a; *Karleskind et al.*, 2011] and in the Mediterranean Sea [*Lévy et al.*, 1999, 2000]. This restratification does not necessarily modify the amplitude of the bloom but modulates spatially the restratification process that occurs at large-scale in February (Figures 7, 5k, and 5l). The entanglement of spatial and temporal variability introduced by the presence of mesoscale structures can be an issue for observational survey [*Resplandy et al.*, 2009]: as described above, surface Chl values that are observed by ocean color satellites do not reflect the integrated value and a higher spatio-temporal resolution in *in-situ* measurements can be necessary to describe accurately the dynamical and biogeochemical fields.

[55] In addition to the restratifying effect, the ageostrophic circulation is associated with enhanced vertical velocities [*Klein et al.*, 2008, Figure 7; *Lévy et al.*, 2010]. The convective input of nutrient is thus completed by the eddy-induced vertical advection that accounts for ~40 – 50% of the nutrient supply during the winter bloom period in the central AS (Table 2 and section 5.1). A similar process of eddy-induced vertical advection of nutrients has been identified in the North-Atlantic subtropical gyre in the eddy-resolving model studies by *Oschlies* [2002b] and *McGillicuddy et al.* [2003].

### 6.2. Eddy-Induced Advection During Summer

[56] As expected from previous observational and modeling studies, the upwelling systems are the major source of nutrients during the SMW period. However, this study is the first to evidence the major role of the vertical eddy-induced advection in supplying nutrients to the upwelling systems off Somalia, Oman and India. During the early stage of the summer bloom period (April to July), the eddy-induced advection supply is tremendously high with contributions up to 60–90% of the nutrients input to the upper layer (Table 2 and section 5.2). This input of nutrients is not exported and is available for primary production (Table 2).

[57] Our model also confirms previous results about the predominant role of lateral eddy-induced advection in exporting nutrients from upwelling systems into the central AS. This eddy-induced transport takes place in the late summer bloom period (August-November) and exports the total amount of nutrients brought to the surface by the mean advection during that period (Table 2 and section 5.2). It is mediated by mesoscale structures that are different in the three upwelling systems.

[58] In our model, nutrient-rich waters upwelled offshore Somalia are advected northward through the Socotra Passage along the coast of the Arabic Peninsula and eastward through the Great Whirl and Socotra Eddy, which finally fuel the CAS (Figure 9e). This result is in agreement with the modeling study of *Kawamiya* [2001] and the work of *Prasanna Kumar et al.* [2001] based on SST data, which concluded that the upwelling off Somalia is a major source of nitrate for the central Arabian Sea.

[59] The most intense eddy-induced transport in the model exports nutrients offshore the upwelling of Oman (Table 2). The ~100 km width mesoscale filaments that develop offshore Oman extend ~500–1000 km into the central AS, in agreement with the numerous studies that described these structures from observations [*Brock et al.*, 1991; *Brink et al.*, 1998; *Flagg and Kim*, 1998; *Manghnani et al.*, 1998; *Lee et al.*, 2000] and models [*Young and Kindle*, 1994; *Keen et al.*, 1997; *Kawamiya*, 2001]. The position of these jets in our model is however relatively steady, whereas altimetry indicates it varies interannually due to the presence of eddies on the shelf prior to the onset of the SWM [*Manghnani et al.*, 1998]. This short-coming could be explained by the model resolution that represents the mesoscale dynamics but does not resolve the sub-mesoscale processes that constrain the mesoscale variability.

[60] The lateral export of nutrient out of the Indian upwelling is mostly mediated by mesoscale eddies of 50–

**Table A1.** Model Prognostic Equations

| Description | Equation | Equation Number |
|---|---|---|
| Nanophytoplankton source/sink | $\frac{\partial P}{\partial t} = (1-\delta^P)\mu^P P - m^P \frac{P}{K_P+P} P - w_p^P P^2 - g^Z(P)Z - g^Z(P)M$ | (A1) |
| Diatoms source/sink | $\frac{\partial D}{\partial t} = (1-\delta^D)\mu^D D - m^D \frac{D}{K_D+D} D - w_p^D D^2 - g^Z(D)Z - g^M(D)M$ | (A2) |
| Microzooplankton source/sink | $\frac{\partial Z}{\partial t} = e^Z(g^Z(P) + g^Z(D) + g^Z(POC_s))Z_1 - r^Z \frac{Z}{K_Z+Z} Z$ | (A3) |
| Mesozooplankton source/sink | $\frac{\partial M}{\partial t} = e^M(g^M(P) + g^M(D) + g^M(Z) + g^M POC_s) + g^M(POC_b))M - r^M \frac{M}{K_M+M} M - m^M M^2$ | (A4) |
| DOC source/sink | $\frac{\partial DOC}{\partial t} = \delta^P \mu^P P + \delta^D \mu^D D + (1-\varepsilon^Z) r^Z \frac{Z}{K_Z+Z} Z + (1-\varepsilon^M) r^M \frac{M}{K_M+M} M + \lambda^\star_{POC} POC_s$ $+ (1-\sigma^Z - e^Z)(1-\gamma^Z)(g^Z(P) + g^Z(D) + g^Z(POC_s))Z$ $+ (1-\sigma^M - e^M)(1-\gamma^M)(g^M(P) + g^M(D) + g^M(Z) + g^M(POC_s) + g^M(POC_b))M$ $- \lambda^\star_{DOC} DOC - \Phi_{agg}^{DOC \to POC_s} - \Phi_{agg}^{DOC \to POC_b}$ | (A5) |
| Small POC source/sink | $\frac{\partial POC_s}{\partial t} = \sigma^Z \left( \sum_N g^Z(N) \right) Z - g^Z(POC_s)Z + (1 - 0.5R_{CaCO3}) \left( m^P \frac{P}{K_P+P} P + w_P^P P^2 \right)$ $+ 0.5 m^D \frac{D}{K_D+D} D + \varepsilon^Z r^Z \frac{Z}{Z_Z+Z} Z - \lambda^\star_{POC} POC_s$ $- w^{POC_s} \frac{\partial POC_s}{\partial z} + \Phi_{agg}^{DOC \to POC_s} - \Phi_{agg}^{POC_s \to POC_b}$ | (A6) |
| Large POC source/sink | $\frac{\partial POC_b}{\partial t} = \sigma^M \left( \sum_N g^M(N) \right) M + \varepsilon^M r^M \frac{M}{K_M+M} M + m^M M^2$ $+ 0.5 R_{CaCO3} \left( m^P \frac{P}{K_P+P} P + w_P^P P^2 \right) + 0.5 m^D \frac{D}{K_D+D} D + w_P^D D^2$ $- \lambda^\star_{POC} POC_b - w^{POC_b} \frac{\partial POC_b}{\partial z} + \Phi_{agg}^{DOC \to POC_b} + \Phi_{agg}^{POC_s \to POC_b}$ | (A7) |
| Nitrate source/sink | $\frac{\partial NO_3}{\partial t} = -\mu_{no3}^P P - \mu_{no3}^D D + Nitrif - Denit$ | (A8) |
| Ammonium source/sink | $\frac{\partial NH_4}{\partial t} = -\mu_{nh4}^P P - \mu_{nh4}^D D + \lambda^\star_{DOC} DOC + (1-\sigma^Z - e^Z)\gamma^Z (g^Z(P) + g^Z(D) + g^Z(POC_s))Z$ $+ (1-\sigma^M - e^M)\gamma^M (g^M(P) + g^M(D) + g^M(Z) + g^M(POC_s) + g^M(POC_b))M$ $- Nitrif + Nfix$ | (A9) |
| Silicate source/sink | $\frac{\partial Si}{\partial t} = -(1-\delta^D)\mu^D (\frac{Si}{C}) D + \lambda_{BSi} * BSi$ | (A10) |
| Chlorophyll prognostic | $\frac{\partial I^{Chl}}{\partial t} = \rho^I_{Chl} (1-\delta^I)\mu^I I - m^I \frac{I}{K_I+I} I^{Chl} - w_p^I I I^{Chl} - g^Z(I)\theta^I_{Chl} Z - g^M(I)\theta^I_{Chl} M$ | (A11) |
| Diatoms silica prognostic | $\frac{\partial D^{Si}}{\partial t} = (1-\delta_2)\mu^D (\frac{Si}{C})^{opt} D - m^D \frac{D}{K_D+D} D^{Si} - w_P^D D D^{Si} - (g^Z(D)Z + g^M(D)M)(\frac{D}{Si} D)$ | (A12) |
| Biogenic silica prognostic | $\frac{\partial BSi}{\partial t} = m^D \frac{D}{K_D+D} D^{Si} + w_P^D D D^{Si} + \left( \frac{D^{Si}}{D} \right) (g^Z(D)Z + g^M(D)M)$ $- \lambda^\star_{BSi} BSi - w^{POC_b} \frac{\partial BSi}{\partial z}$ | (A13) |

100 km and the 10–50 km width filaments wrapped around them. These summer structures captured both by SeaWiFS and by the model have not been described as extensively as their western and wintertime counterparts. It is however well known that mesoscale activity in the form of eddies and filaments is a constant feature of eastern boundary upwelling, which mostly arises from the instability of the coastal current and the frontal area [*Batteen*, 1997; *Leth and Middleton*, 2004; *Blanke et al.*, 2005; *Capet et al.*, 2008]. Eddy induced lateral transport of nutrients is not specific to upwelling areas, and has been suggested to contribute significantly to the nutrient budget in the oligotrophic subtropical gyre of the North Atlantic *Oschlies* [2002b]. In addition to the eddy-induced lateral transport by these mesoscale structures, our model suggests that the vertical advection associated with them is the major source of nitrate in the eastern central AS (Figure 9 and section 5.3).

## 7. Conclusions

[61] Numerous *in-situ* observations and model results highlighted the signature of the mesoscale dynamics on the biological response in the Arabian Sea [*Flagg and Kim*, 1998; *Kim et al.*, 2001; *Marra and Barber*, 2005; *Wiggert et al.*, 2005], suggesting these small-scale processes could have a key role at the basin scale. By using a biophysical model resolving the mesoscale (1/12° horizontal resolution), we identify and quantify the contribution of mesoscale

**Table A2.** Model Diagnostic Equations

| Description | Equation |
|---|---|
| Phytoplankton $I$ production | $\mu^I = \mu_I(1 - e^{\frac{\alpha^I \left(\frac{Chl}{C}\right)^I PAR}{\mu_I L^I_{\lim}}})\, L^I_{\lim}$ with $\mu_I = ab^{cT}$ and $T$ the temperature |
| Limitation terms | $L^P_{\lim} = L^P_{no3} + L_{nh4}{}^P L^D_{\lim} = \min(L^D_{no3} + L^D_{nh4}, L^D_{si})$ |
| | $L^I_{no3} = \frac{K^I_{nh4} NO_3}{K^I_{no3} K^I_{nh4} NO_3 + K^I_{no3} NH_4}\, L^I_{nh4} = \frac{K^I_{no3} NH_4}{K^I_{no3} K^I_{nh4} + K^I_{nh4} NO_3 + K^I_{no3} NH_4}\, L^D_{si} = \frac{Si}{K^D_{Si} + Si}$ |
| Nutrient-stress sinking rate | $w^D_p = w^{\min}_p + w^{\max}_p \times (1 - L^D_{\lim})$ |
| Zooplankton grazing on reservoir $N$ | $g^Z(N) = g^Z \frac{Zp^Z_N N}{K^Z_G} + \sum_Y \left(p^Z_Y Y\right)$, with Y all grazed reservoirs |
| Mesozooplankton grazing on reservoir $N$ | $g^M(N) = g^M \frac{p^M_N N}{K^M_G + \sum_Y \left(p^M_Y Y\right)}$, with Y all grazed reservoirs |
| Flux feeding | $g^M(POC_b) = g^M_{FF} w^{POCb} POC_b$ |
| Remineralization rate | $\lambda_{DOC}{}^* = \lambda_{DOC} L^{bac}_{\lim}\, 0.7(Z + 2M)\min(1, \frac{120m}{z})$ with $\mathrm{L}^{bac}_{\mathrm{Lim}} = L^P_{\lim} \frac{DOC}{K^{bac}_{DOC} + DOC}$ |
| Aggregation processes | $\Phi^{DOC \to POCs}_{agg} = \phi^{DOC}_1$ shear $DOC^2 + \phi^{DOC}_2$ shear $DOCPOC_s$ |
| | $\Phi^{DOC \to POCb}_{agg} = \phi^{DOC}_3$ shear $DOCPOC_b$ |
| | $\Phi^{POCs \to POCb}_{agg} = \phi^{POCs}_1$ shear $POC_s^2 + \phi^{POCs}_2$ shear $POC_b POC_s + \phi_3{}^{POCs} POC_s{}^2 + \phi_4{}^{POCs} POC_b POC_s$ |
| $POC_b$ sinking speed | $w^{POC} = w^{POC}_{\min} + (w^{POC}_{\max} - w^{POC}_{\min})\max(0, \frac{z - z_{mel}}{2000m})$ |
| Nitrification | $Nitrif = \lambda_{NH4} \frac{1}{1 + PAR}(1 - \Delta(O_2))NH_4$ |
| Denitrification | $Denit = R_{NO3} \lambda^*_{DOC} \Delta(O_2) DOC$ |
| | with $\Delta(O_2) = \min\left(1, 0.4 \frac{\max(0, 6 - O_2)}{O_2^{\min} + O_2}\right)$ |
| Nitrogen fixation | $Nfix = \frac{\int_{xyz,t} Denit}{\int_{xyz,t} Nfix_p ot} Nfix_{pot}$ with $Nfix_{pot} = \mu^P \max(0, \mu_P - \mu_P(20°\mathrm{C}))(1 - L^P_{no3} - L^P_{nh4}))$ |
| Biogenic Si dissolution | $\lambda^*_{BSi} = \lambda_{BSi}\left[0.225\left(1 + \frac{T}{15}\right) Si_{sat} + 0.775\left(\left(1 + \frac{T}{400}\right)^4 Si_{sat}\right)^9\right]$ |
| | with $Si_{sat} = \frac{10^{6.44 - \frac{968}{T + 273.15}} - Si}{10^{6.44 - \frac{968}{T + 273.15}}}$ |
| Energy assimilation efficiency | $\rho^I_{Chl} = \theta^I_{Chl,\max} \frac{144 \mu^I I}{\alpha^I \times PAR \times I^{Chl}}$ |
| Si:C ratio | $\left(\frac{Si}{C}\right)^{opt} = \min\left(1, \left(0.14 L^D_{Si}\left(5.4 e^{F^{Si}_{Lim}} + 1.13\right)\right)\right) \times \left(1 + 3\left(\frac{\max(0, Si - Si_{\min})}{K^2_{Si} + Si}\right)\right)$ |
| | with $F^{Si}_{\lim} = \min\left(\left(1 - e^{\frac{\alpha^D \left(\frac{Chl}{C}\right)^D PAR}{\mu_D L^D_{\lim}}}\right), L^P_{no3} + L^P_{nh4}\right)$ |

processes during the summer and winter blooms. We argue here that mesoscale dynamics regulate the phytoplankton biomass by modulating both the nutrient input to the surface layer and the mixed layer depth. Resolving the mesoscale improves the simulated surface chlorophyll patterns and increases the integrated primary production and export, in better agreement with estimates derived from satellite data and *in-situ* measurements than previous model estimates at lower resolution [*Kawamiya*, 2001; *Wiggert et al.*, 2006; *Koné et al.*, 2009]. The impact of mesoscale processes is however highly dependent on the mean ocean dynamics and hence varies widely between the winter and summer monsoons.

[62] Dominant processes identified during the summer bloom period in this study are:

[63] 1. Mesoscale processes highly modulate the input of nutrients in upwelling regions and in the central Arabian Sea.

[64] 2. In upwelling regions, the eddy-induced vertical advection is the primary source of nutrients to the upper layer (60–90%) during the early stage of the summer bloom (April-July). Later in the season, the eddy-induced lateral advection exports nutrients out of upwelling regions via filamentary structures and thus sustains the bloom in the central Arabian Sea.

[65] 3. The central Arabian Sea supply in nutrients presents a east/west contrast: nutrients are primarily supplied by eddy-induced lateral advection from the upwelling systems off Somalia and Oman in the west, whereas eddy-induced vertical advection is the major source of nutrients in the east.

**Table A3.** Model Parameters

| Parameter | Units | Value | Description |
|---|---|---|---|
| | | *Phytoplankton* | |
| $a$ | $d^{-1}$ | 0.66 | Growth rate at 0°C |
| $b$ | – | 1.066 | Temperature sensitivity of growth |
| $c$ | °C | 1 | Temperature dependence of growth |
| $\alpha_P$, $\alpha_D$ | $(W\ m^{-2})^{-1}\ d^{-1}$ | 3, 3 | initial slope of P-I curve |
| $\delta_P$, $\delta_D$ | – | 0.05, 0.05 | exudation of DOC |
| $K_{nh_4}^P$, $K_{nh_4}^D$ | $\mu$mol N $l^{-1}$ | 0.013, 0.065 | Half-saturation constant for ammonium |
| $K_{no_3}$ , $K_{no_3}$ | $\mu$mol N $l^{-1}$ | 1.3, 0.26 | Half-saturation constant for nitrate |
| $K_{si}^D$ | $\mu$mol Si $l^{-1}$ | 2 | Half saturation constant for silicate |
| $P_{\max}$ | $\mu$mol C $l^{-1}$ | 1 | Maximum concentration of small nanophytoplankton |
| $D_{\max}$ | $\mu$mol C $l^{-1}$ | 0.5 | Maximum concentration of diatoms |
| $m_P$ | $d^{-1}$ | 0.01 | Phytoplankton mortality rate |
| $w_P$ | $d^{-1}$ mol $C^{-1}$ | 0.01 | Quadratic mortality of phytoplankton |
| $w_P^{\max}$ | $d^{-1}$ mol $C^{-1}$ | 0.02 | Maximum quadratic mortality of diatoms |
| $K_P$ | $\mu$ mol C $l^{-1}$ | 0.1 | Half-saturation constant for mortality |
| $\theta_{chl,\max}^P$, $\theta_{chl,\max}^D$ | mg Chl mg $C^{-1}$ | 0.033, 0.05 | Maximum Chl/C ratios of phytoplankton |
| $K_{Si}^2$ | $\mu$ mol $Sil^{-1}$ | 5 | Half saturation constant for Si/C increase |
| | | *Zooplankton* | |
| $\varepsilon$ | – | 0.35,0.35 | Zooplankton growth efficiency |
| $\sigma$ | – | 0.3,0.3 | Fecal pellets production |
| $g_M$ | $d^{-1}$ | 4,0.7 | Maximum grazing rate |
| $g_{FF}$ | $(m\ mol\ l^{-1})^{-1}$ | $5\ 10^3$ | Maximum flux feeding rate |
| $K_G$ | $\mu$ mol $Cl^{-1}$ | 20, 20 | Half-saturation constant for grazing |
| $p_P^Z$, $\gamma_P$ | – | 0.5, 0.2 | Preferences for nanophytoplankton |
| $p_D^Z$, $\gamma_D$ | – | 0.5, 1 | Preferences for diatoms |
| $p_{POC}^Z$, $\gamma_{POC}$ | – | 0., 0.2 | Preferences for $POC_s$ |
| $\gamma_Z$ | – | 1. | Preference for microzooplankton |
| $P_{\min}$ | $\mu$ mol $Cl^{-1}$ | 0.1 | Minimum available concentration of nanophytoplankton |
| $m^M$ | $(\mu\ mol\ Cl^{-1})^{-1}d^{-1}$ | 0.03 | Mesozooplankton mortality |
| $r$ | $d^{-1}$ | 0.03, 0.008 | Excretion rate |
| $K$ | $\mu$ mol $Cl^{-1}$ | 0.1 | Half-saturation constant for excretion |
| $\epsilon$ | - | 0.5, 0.5 | |
| $(\frac{Fe}{C})^{zoo}$ | $\mu$ mol Fe mol $C^{-1}$ | 3 | Fe/C ratio of zooplankton |
| | | *Organic Matter* | |
| $\lambda_{DOC}$ | $d^{-1}$ | 0.3 | Remineralization rate of DOC |
| $K_{DOC}^{bac}$ | $\mu$ mol C $l^{-1}$ | 417 | Half-saturation constant for DOC remin. |
| $\lambda_{POC}$ | $d^{-1}$ | 0.025 | Degradation rate of POC |
| $w_{\min}$ | $md^{-1}$ | 3, 50 | Minimum sinking speed of POC |
| $w_{\max}$ | $md^{-1}$ | 200 | Maximum sinking speed of $POC_b$ |
| $\Phi_1^{DOC}$, $\Phi_1^{DOC}\Phi_2^{DOC}$ | $(mol\ C\ l^{-1})^{-1}$ | 80,698 | Aggregation rates for $DOC \rightarrow POC_s$ |
| $\Phi_3^{DOC}$ | $(mol\ C\ l^{-1})^{-1}$ | 10,500 | Aggregation rates for $DOC \rightarrow POC_b$ |
| $\Phi_1^{POCs}$, $\Phi_1^{POCs}$ | $(mol\ C\ l^{-1})^{-1}$ | 940, 10,540 | Aggregation rates for $POC_s \rightarrow POC_b$ |
| $\Phi_3^{POCs}$, $\Phi_4^{POCs}$ | $(mol\ C\ l^{-1})^{-1}$ | 0.66, 0 | Aggregation rates for $POC_s \rightarrow POC_b$ |
| $\lambda_{BSi}$ | $d^{-1}$ | 0.015 | Dissolution rate of BSi |
| $\lambda_{NH_4}$ | $d^{-1}$ | 0.05 | Maximum nitrification rate |
| $O_2^{\min}$ | $\mu$ mol $O_2$ $l^{-1}$ | 1 | Half saturation constant for denitrification |
| | | *Stoichiometric Ratios* | |
| $R_{NO_3}$ | mol C mol $N^{-1}$ | −0.8 | C/N ratio of denitrification |
| $R_{CaCO3}$ | – | 0.4 | Maximum rain ratio |

[66] In contrast, the processes highlighted for the winter bloom period are:

[67] 1. The bloom is triggered by convective mixing. The convective input of nutrients lowers the phytoplankton growth limitation increasing the primary production, whereas the light limitation is of second importance.

[68] 2. In addition to convective mixing, eddy-induced vertical advection within mesoscale eddies and filaments accounts for 40–50% of the nutrients supplied to the upper layer.

[69] 3. Mesoscale structures modulate spatially and temporally the mixed layer depth and the restratification process that occurs in February in the central Arabian Sea. This is not very likely to modify the bloom amplitude but could be a challenge for observational programs.

[70] The most obvious variability in the bloom dynamics over the Arabian Sea is associated with the seasonal cycle and the monsoonal reversal of winds. This work emphasizes how mesoscale dynamics modulates this seasonal cycle and in particular its major role on the blooms onset and regulation. We think it is important to account for these processes to improve the representation and the comprehension of the biogeochemistry in the area. Notably, the influence of mesoscale dynamics on the annual primary production and export could modulate the mechanisms regulating the intense oxygen minimum zone that covers the Arabian Sea

[*Naqvi et al.*, 1998]. Another interesting question that arises is how this mesoscale-induced variability compares and relates to the interannual variability associated with climate mode. Indeed, another strong contribution to the biogeochemical variability in the Arabian Sea is due to interannual variability [*Brock and McClain*, 1992; *Wiggert et al.*, 2002, 2005] associated either with either with El Niño remote forcing or with the Indian Ocean Dipole [*Saji et al.*, 1999; *Webster et al.*, 1999; *Murtugudde et al.*, 2000].

## Appendix A: Model Equations

[71] The biogeochemical model used in this study is based on the intermediate complexity biogeochemical model Pelagic Interaction Scheme for Carbon and Ecosystem Studies (PISCES), simplified from 24 to 16 tracers, taking out compartments related to the cycling of phosphate and iron. Prognostic equations and diagnostic equations for these 16 compartments are presented in Tables A1 and A2, respectively, while model parameters used in our model configuration are detailed in Table A3.

[72] **Acknowledgments.** We sincerely thank the NEMO system team for their development and maintenance of the NEMO ocean general circulation model. Thanks to Charles Deltel for his contribution concerning the regional model configuration. Support was provided by the Twisted (ToWard Integration of Subgrid Turbulence in Ecosystem Dynamics) program. The Chl data were provided by the SeaWiFS Project and NASA's DAAC. The altimeter products were produced by Ssalto/Duacs and distributed by AVISO with support from Cnes (Centre National d'Etudes Spatiales). Sea Surface Temperature TMI data are produced by Remote Sensing Systems and sponsored by the NASA Earth Science MEaSUREs DISCOVER Project and available at www.remss.com.

## References

Al Saafani, M. A., S. S. C. Shenoi, D. Shankar, M. Aparna, J. Kurian, F. Durand, and P. N. Vinayachandran (2007), Westward movement of eddies into the Gulf of Aden from the Arabian Sea, *J. Geophys. Res.*, *112*, C11004, doi:10.1029/2006JC004020.

Antoine, D., J.-M. André, and A. Morel (1996), Oceanic primary production: 2. Estimation at global scale from satellite (Coastal Zone Color Scanner) chlorophyll, *Global Biogeochemical Cycles*, *10*(1), 57–69.

Aumont, O., and L. Bopp (2006), Globalizing results from ocean in situ iron fertilization studies, *Global Biogeochem. Cycles*, *20*, GB2017, doi:10.1029/2005GB002591.

Aumont, O., E. Maier-Reimer, S. Blain, and P. Monfray (2003), An ecosystem model of the global ocean including Fe, Si, P colimitations, *Global Biogeochem. Cycles*, *17*(2), 1060, doi:10.1029/2001GB001745.

Banse, K. (1968), Hydrography of the Arabian Sea shelf of India and Pakistan and effects on demersal fishes, *Deep Sea Res. Oceanogr. Abstr.*, *15* (1), 45–48, IN7–IN10, 49–79, doi:10.1016/0011-7471(68)90028-4.

Banse, K. (1987), Seasonality of phytoplankton chlorophyll in the central and northern Arabian Sea, *Deep Sea Res., Part I*, *34*(5–6), 713–723, doi:10.1016/0198-0149(87)90032-X.

Banse, K. (1994), On the coupling of hydrography, phytoplankton, zooplankton, and settling organic particles offshore in the Arabian Sea, *Proc. Indian Acad. Sci. Earth Planet. Sci.*, *103*, 125–161.

Banse, K., and D. C. English (2000), Geographical differences in seasonality of CZCS-derived phytoplankton pigment in the Arabian Sea for 1978–1986, *Deep Sea Res., Part II*, *47*, 1623–1677.

Banse, K., and C. McClain (1986), Winter blooms of phytoplankton in the Arabian Sea as observed by the Coastal Zone Color Scanner, *Mar. Ecol. Prog. Ser.*, *34*, 201–211.

Barber, R. T., J. Marra, R. C. Bidigare, L. A. Codispoti, D. Halpern, Z. Johnson, M. Latasa, R. Goericke, and S. L. Smith (2001), Primary productivity and its regulation in the Arabian Sea during 1995, *Deep Sea Res., Part II*, *48*(6–7), 1127–1172, doi:10.1016/S0967-0645(00)00134-X.

Barnier, B., et al. (2006), Impact of partial steps and momentum advection schemes in a global ocean circulation model at eddy permitting resolution, *Ocean Dyn.*, *56*, 543–567, doi:10.1007/s10236-006-0082-1.

Batteen, M. L. (1997), Wind-forced modeling studies of currents, meanders and eddies in the California Current System, *J. Geophys. Res.*, *28*, 2199–2221.

Bauer, S., G. L. Hitchcock, and D. B. Olson (1991), Influence of monsoonally-forced Ekman dynamics upon the surface-layer depth and plankton biomass distribution in the Arabian Sea, *Deep Sea Res.*, *38*, 531–553.

Behrenfeld, M. J. (2010), Abandoning Sverdrup's critical depth hypothesis on phytoplankton blooms, *Ecology*, *91*(4), 977–989.

Behrenfeld, M. J., and P. Falkowski (1997), Photosynthetic rates derived from satellite-based chlorophyll concentration, *Limnol. Oceanogr.*, *42*, 1–20.

Bernie, D., E. Guilyardi, G. Madec, J. Slingo, and S. Woolnough (2007), Impact of resolving the diurnal cycle in an ocean-atmosphere GCM. Part 1: A diurnally forced OGCM, *Clim. Dyn.*, *29*, 575–590, doi:10.1007/s00382-007-0249-6.

Blanke, B., and P. Delecluse (1993), Variability of the tropical Atlantic Ocean simulated by a general circulation model with two different mixed-layer physics, *J. Phys. Oceanogr.*, *23*, 1363–1388.

Blanke, B., S. Speich, A. Bentamy, C. Roy, and B. Sow (2005), Modeling the structure and variability of the southern Benguela upwelling using QuikSCAT wind forcing, *J. Geophys. Res.*, *110*, C07018, doi:10.1029/2004JC002529.

Bourdallé-Badie, R., and A. -M. Treguier (2006), A climatology of runoff for the global ocean-ice model ORCA025, *Mercator Rep., MOO-RP-425-366-MER*, Mercator-Ocean, Toulouse, France.

Bower, A. S., D. M. Fratantoni, W. E. Johns, and H. Peters (2002), Gulf of Aden eddies and their impact on Red Sea Water, *Geophys. Res. Lett.*, *29* (21), 2025, doi:10.1029/2002GL015342.

Brandt, P., M. Dengler, A. Rubino, D. Quadfasel, and F. Schott (2003), Intraseasonal variability in the southwestern Arabian Sea and its relation to the seasonal circulation, *Deep Sea Res., Part II*, *50*(12–13), 2129–2141, doi:10.1016/S0967-0645(03)00049-3.

Brink, K., R. Arnone, P. Coble, C. Flagg, B. Jones, J. Kindle, C. Lee, and D. Phinney (1998), Monsoons boost biological productivity in Arabian Sea, *Eos Trans. AGU*, *79*, 165.

Brock, J. C., and C. R. McClain (1992), Interannual variability in phytoplankton blooms observed in the northwestern Arabian Sea during the Southwest Monsoon, *J. Geophys. Res.*, *97*(C1), 733–750.

Brock, J. C., C. R. McClain, M. E. Luther, and W. W. Hay (1991), The phytoplankton bloom in the northwestern Arabian Sea during the Southwest Monsoon of 1979, *J. Geophys. Res.*, *96*, 20,623–20,642.

Brodeau, L., B. Barnier, T. Penduff, A. -M. Tréguier, and S. Gulev (2009), An ERA40 based atmospheric forcing for global ocean circulation models, *Ocean Modell.*, *31*, 88–104, doi:10.1016/j.ocemod.2009.10.005.

Bruce, J. G., D. R. Johnson, and J. C. Kindle (1994), Evidence for eddy formation in the eastern Arabian Sea during the northeast monsoon, *J. Geophys. Res.*, *99*, 7651–7664.

Capet, X., F. Colas, P. Penven, P. Marchesiello, and J. C. McWilliams (2008), Eddies in eastern boundary subtropical upwelling systems, in *Ocean Modeling in an Eddying Regime*, *Geophys. Monogr. Ser.*, vol. 177, edited by M. W. Hecht and H. Hasumi, pp. 131–148, AGU, Washington, D. C.

Chelton, D. B., R. A. deSzoeke, M. G. Schlax, K. E. Naggar, and N. Siwertz (1998), Geographical variability of the first-baroclinic Rossby radius of deformation, *J. Phys. Oceanogr.*, *28*, 433–460.

de Boyer Montégut, C., G. Madec, A. S. Fischer, A. Lazar, and D. Iudicone (2004), Mixed layer depth over the global ocean: An examination of profile data and a profile-based climatology, *J. Geophys. Res.*, *109*, C12003, doi:10.1029/2004JC002378.

Dickey, T., J. Marra, D. E. Sigurdson, R. A. Weller, C. S. Kinkade, S. E. Zedler, J. D. Wiggert, and C. Langdon (1998), Seasonal variability of bio-optical and physical properties in the Arabian Sea: October 1994–October 1995, *Deep Sea Res., Part II*, *45*(10–11), 2001–2025, doi:10.1016/S0967-0645(98)00061-7.

Dutkiewicz, S., M. J. Follows, and P. Parekh (2005), Interactions of the iron and phosphorus cycles: A three-dimensional model study, *Global Biogeochem. Cycles*, *19*, GB1021, doi:10.1029/2004GB002342.

Findlater, J. (1969), A major low-level air current near the Indian Ocean during the northern summer, *Q. J. R. Meteorol. Soc.*, *95*, 362–380.

Fischer, A. S., R. A. Weller, D. L. Rudnick, C. C. Eriksen, C. M. Lee, K. H. Brink, C. A. Fox, and R. R. Leben (2002), Mesoscale eddies, coastal upwelling, and the upper-ocean heat budget in the Arabian Sea, *Deep Sea Res., Part II*, *49*(12), 2231–2264, doi:10.1016/S0967-0645(02)00036-X.

Flagg, C., and H. -S. Kim (1998), Upper ocean currents in the northern Arabian Sea from shipboard ADCP measurements during the 1994–1996 U.S. JGOFS and ONR programs, *Deep Sea Res., Part II*, *45*, 1917–1960.

Friedrichs, M. A. M., R. Hood, and J. D. Wiggert (2006), Ecosystem model complexity versus physical forcing: Quantification of their relative impact with assimilated Arabian Sea data, *Deep Sea Res., Part II*, *53*, 576–600.

Garrison, D. L., M. M. Gowing, and M. P. Hughes (1998), Nano- and microplankton in the northern Arabian Sea during the Southwest

Monsoon, August-September 1995: A US-JGOFS study, *Deep Sea Res., Part II*, *45*(10–11), 2269–2299, doi:10.1016/S0967-0645(98)00071-X.

Gauns, M., M. Madhupratap, N. Ramaiah, R. Jyothibabu, V. Fernandes, J. T. Paul, and S. P. Kumar (2005), Comparative accounts of biological productivity characteristics and estimates of carbon fluxes in the Arabian Sea and the Bay of Bengal, *Deep Sea Res., Part II*, *52*(14–15), 2003–2017, doi:10.1016/j.dsr2.2005.05.009.

Griffies, S. M., et al. (2009), Coordinated Ocean-ice Reference Experiments (COREs), *Ocean Modell.*, *26*(1–2), 1–46, doi:10.1016/j.ocemod.2008.08.007.

Hitchcock, G. L., E. L. Key, and J. Masters (2000), The fate of upwelled waters in the Great Whirl, August 1995, *Deep Sea Res., Part II*, *47*(7–8), 1605–1621, doi:10.1016/S0967-0645(99)00156-3.

Honjo, S., J. Dymond, W. Prell, and V. Ittekkot (1999), Monsoon-controlled export fluxes to the interior of the Arabian Sea, *Deep Sea Res., Part II*, *46*(8–9), 1859–1902, doi:10.1016/S0967-0645(99)00047-8.

Karleskind, P., M. Lévy, and L. Mémery (2011), Modifications of mode water properties by sub-mesoscales in a bio-physical model of the northeast Atlantic, *Ocean Modell.*, *39*, 47–60, doi:10.1016/j.ocemod.2010.12.003.

Kawamiya, M. (2001), Mechanism of offshore nutrient supply in the western Arabian Sea, *J. Mar. Res.*, *59*, 675–696.

Kawamiya, M., and A. Oschlies (2003), An eddy-permitting, coupled ecosystem-circulation model of the Arabian Sea: Comparison with observations, *J. Mar. Syst.*, *38*(3–4), 221–257, doi:10.1016/S0924-7963(02)00241-5.

Keen, T., J. Kindle, and D. Young (1997), The interaction of Southwest Monsoon upwelling, advection and primary production in the northwest Arabian Sea, *J. Mar. Syst.*, *13*, 61–82.

Kim, H. -S., C. N. Flagg, and S. Howden (2001), Northern Arabian Sea variability from TOPEX/Poseidon altimetry data, an extension of the JGOFS/ONR shipboard ADCP study, *Deep Sea Res., Part II*, *48*, 1069–1096.

Klein, P., B. L. Hua, G. Lapeyre, X. Capet, S. L. Gentil, and H. S. Sasaki (2008), Upper ocean turbulence from high 3-d resolution simulations, *J. Phys. Oceanogr.*, *38*, 1748–1763.

Kobayashi, T., and T. Suga (2006), The Indian Ocean HydroBase: A high-quality climatological dataset for the Indian Ocean, *Prog. Oceanogr.*, *68* (1), 75–114, doi:10.1016/j.pocean.2005.07.001.

Koné, V., O. Aumont, M. Lévy, and L. Resplandy (2009), Physical and biogeochemical controls of the phytoplankton seasonal cycle in the Indian Ocean: A modeling study, in *Indian Ocean Biogeochemical Processes and Ecological Variability*, *Geophys. Monogr. Ser.*, vol. 185, edited by J. D. Wiggert et al., pp. 147–166, AGU, Washington, D. C.

Kravtsova, V., V. Mikhailov, and N. Efremova (2009), Variations of the hydrological regime, morphological structure, and landscapes of the Indus River delta (Pakistan) under the effect of large-scale water management measures, *Water Resour.*, *36*, 365–379, doi:10.1134/S0097807809040010.

Lapeyre, G., P. Klein, and B. Hua (2006), Oceanic restratification forced by surface frontogenesis, *J. Phys. Oceanogr.*, *36*, 1577–1590.

Large, W. G., and S. G. Yeager (2004), Diurnal to decadal global forcing for ocean and sea-ice models, *NCAR Tech. Note, TN-460+STR*, 22 pp., Natl. Cent. for Atmos. Res., Boulder, Colo.

Lee, C., et al. (1998), Particulate organic carbon fluxes: Compilation of results from the 1995 US JGOFS Arabian Sea Process Study, *Deep Sea Res., Part II*, *45*(10–11), 2489–2501, doi:10.1016/S0967-0645(98)00079-4.

Lee, C. M., B. H. Jones, K. H. Brink, and A. S. Fischer (2000), The upper-ocean response to monsoonal forcing in the Arabian Sea: Seasonal and spatial variability, *Deep Sea Res., Part II*, *47*, 1177–1226.

Leth, O., and J. F. Middleton (2004), A mechanism for enhanced upwelling off central Chile: Eddy advection, *J. Geophys. Res.*, *109*, C12020, doi:10.1029/2003JC002129.

Levitus, S., T. Boyer, M. Conkright, T. O'Brian, J. Antonov, C. Stephens, L. Stathopolos, D. Johnson, and R. Gelfeld (1998), World Ocean Database 1998, *Tech. Rep., NESDID18*, NOAA, Silver Spring, Md.

Lévy, M., L. Mémery, and G. Madec (1999), The onset of the spring bloom in the MEDOC area: Mesoscale spatial variability, *Deep Sea Res., Part I*, *46*, 1137–1160, doi:10.1016/S0967-0637(98)00105-8.

Lévy, M., L. Mémery, and G. Madec (2000), Combined effects of mesoscale processes and atmospheric high-frequency variability on the spring bloom in the MEDOC area, *Deep Sea Res., Part I*, *47*, 27–53, doi:10.1016/S0967-0637(99)00051-5.

Lévy, M., P. Klein, and A.-M. Treguier (2001), Impacts of sub-mesoscale physics on phytoplankton production and subduction, *J. Mar. Res.*, *59*, 535–565, doi:10.1357/002224001762842181.

Lévy, M., D. Shankar, J.-M. André, S. S. C. Shenoi, F. Durand, and C. de Boyer Montégut (2007), Basin-wide seasonal evolution of the Indian Ocean's phytoplankton blooms, *J. Geophys. Res.*, *112*, C12014, doi:10.1029/2007JC004090.

Lévy, M., P. Klein, A.-M. Tréguier, D. Iovino, G. Madec, S. Masson, and K. Takahashi (2010), Modifications of gyre circulation by sub-mesoscale physics, *Ocean Modell.*, *34*, 1–15, doi:10.1016/j.ocemod.2010.04.001.

Lierheimer, L. J., and K. Banse (2002), Seasonal and interannual variability of phytoplankton pigment in the Laccadive (Lakshadweep) Sea as observed by the Coastal Zone Color Scanner, *Proc. Ind. Acad. Sci. Earth Planet. Sci.*, *111*, 163–185.

Ludwig, W., J. L. Probst, and S. Kempe (1996), Predicting the oceanic input of the organic carbon by continental erosion, *Global Biogeochem. Cycles*, *10*, 23–41.

Lumpkin, R., and Z. Garraffo (2005), Evaluating the decomposition of tropical Atlantic drifter observations, *J. Atmos. Oceanic Technol.*, *22*, 1403–1415.

Madec, G. (2008), NEMO, the ocean engine, *Note du Pole de Model.*, *27*, Inst. Pierre-Simon Laplace, Paris. [Available at http://www.nemo-ocean.eu/About-NEMO/Reference-manuals].

Madhupratap, S. P. K., P. M. A. Bhattathiri, M. D. Kumar, S. Raghukumar, K. K. C. Nair, and N. Ramaiah (1996), Mechanism of the biological response to winter cooling in the northern Arabian Sea, *Nature*, *384*, 549–552.

Manghnani, V., J. M. Morrison, T. S. Hopkins, and E. Böhm (1998), Advection of upwelled waters in the form of plumes off Oman during the Southwest Monsoon, *Deep Sea Res., Part II*, *45*, 2027–2052.

Marra, J., and R. T. Barber (2005), Primary productivity in the Arabian Sea: A synthesis of JGOFS data, *Prog. Oceanogr.*, *65*(2–4), 159–175, doi:10.1016/j.pocean.2005.03.004.

Marra, J., T. D. Dickey, C. Ho, C. S. Kinkade, D. E. Sigurdson, R. A. Weller, and R. T. Barber (1998), Variability in primary production as observed from moored sensors in the central Arabian Sea in 1995, *Deep Sea Res., Part II*, *45*(10–11), 2253–2267, doi:10.1016/S0967-0645(98)00070-8.

McCreary, J. P., K. E. Kohler, R. R. Hood, and D. B. Olson (1996), A four-component ecosystem model of biological activity in the Arabian Sea, *Prog. Oceanogr.*, *37*(3–4), 193–240, doi:10.1016/S0079-6611(96)00005-5.

McGillicuddy, D. J., Jr., L. A. Anderson, S. C. Doney, and M. E. Maltrud (2003), Eddy-driven sources and sinks of nutrients in the upper ocean: Results from a 0.1° resolution model of the North Atlantic, *Global Biogeochem. Cycles*, *17*(2), 1035, doi:10.1029/2002GB001987.

Moffett, J. W., T. J. Goepfert, and S. W. A. Naqvi (2007), Reduced iron associated with secondary nitrite maxima in the Arabian Sea, *Deep Sea Res., Part I*, *54*, 1341–1349.

Molines, J. -M., B. Barnier, T. Penduff, L. Brodeau, A.-M. Treguier, S. Theetten, and G. Madec (2006), Definition of the global 1/2° experiment with CORE forcing, ORCA05-G50, *Rep. LEGI-DRA-1-11-2006*, Lab. des Ecoulements Géophys.et Ind., Grenoble, France.

Moore, J. K., S. C. Doney, and K. Lindsay (2004), Upper ocean ecosystem dynamics and iron cycling in a global three-dimensional model, *Global Biogeochem. Cycles*, *18*, GB4028, doi:10.1029/2004GB002220.

Murtugudde, R. J., P. McCreary, and A. J. Busalacchi (2000), Oceanic processes associated with anomalous events in the Indian Ocean with relevance to 1997–1998, *J. Geophys. Res.*, *105*, 3295–3306.

Naqvi, S. W. A., H. Yoshinari, T. Naik, D. A. Jayakumar, M. A. Altabet, P. Narvekar, A. Devol, J. A. Brandes, and L. A. Codispoti (1998), Budgetary and biogeochemical implications of $N_2O$ isotope signatures in the Arabian Sea, *Nature*, *394*(6692), 462–464.

Nurser, A. J. G., and J. W. Zhang (2000), Eddy-induced mixed layer shallowing and mixed layer/thermocline exchange, *J. Geophys. Res.*, *105* (C9), 851–868.

Olascoaga, M. J., N. Idrisi, and A. Romanou (2005), Biophysical isopycnic-coordinate modelling of plankton dynamics in the Arabian Sea, *Ocean Modell.*, *8*, 55–80.

Oschlies, A. (2002a), Improved representation of upper ocean dynamics and mixed layer depths in a model of the north atlantic on switching from eddy-permitting to eddy-resolving grid resolution, *J. Phys. Oceanogr.*, *32*, 2277–2298.

Oschlies, A. (2002b), Can eddies make ocean deserts bloom?, *Global Biogeochem. Cycles*, *16*(4), 1106, doi:10.1029/2001GB001830.

Pacanowski, R., and A. Gnanadesikan (1998), Transient response in a z-level ocean model that resolves topography with partial cells, *Mon. Weather Rev.*, *126*, 3248–3270.

Penduff, T., M. Juza, L. Brodeau, G. C. Smith, B. Barnier, J. -M. Molines, and A.-M. Treguier (2009), Impact of model resolution on sea-level variability characteristics at various space and time scales: Insights from four DRAKKAR global simulations and the AVISO altimeter data, *Ocean Sci. Discuss.*, *6*, 1–32.

Prasanna Kumar, S., and J. Narvekar (2005), Seasonal variability of the mixed layer in the central Arabian Sea and its implication on nutrients and primary productivity, *Deep Sea Res., Part II*, *52*, 1848–1861.

Prasanna Kumar, S., N. Ramaiah, M. Gauns, V. V. S. S. Sarma, P. M. Muraleedharan, S. Raghukumar, M. D. Kumar, and M. Madhupratap (2001), Physical forcing of biological productivity in the northern Arabian Sea during the Northeast Monsoon, *DeepSea Res., Part II*, *48* (6–7), 1115–1126, doi:10.1016/S0967-0645(00)00133-8.

Rao, R., R. Molinari, and J. Festa (1989), Evolution of the climatological near-surface thermal structure of the tropical Indian Ocean: 1. Description of mean monthly mixed layer depth, and sea surface temperature, surface current, and surface meteorological fields, *J. Geophys. Res.*, *94*, 10,801–10,815.

Resplandy, L., M. Lévy, F. d'Ovidio, and L. Merlivat (2009), Impact of submesoscale variability in estimating the air-sea CO2 exchange: Results from a model study of the POMME experiment, *Global Biogeochem. Cycles*, *23*, GB1017, doi:10.1029/2008GB003239.

Saji, N. H., B. N. Goswami, P. N. Vinayachandran, and T. Yamagata (1999), A dipole mode in the tropical Indian Ocean, *Nature*, *401*, 360–363.

Schott, F. A., and J. P. McCreary (2001), The monsoon circulation of the Indian Ocean, *Prog. Oceanogr.*, *51*, 1–123.

Schott, F. A., J. Fischer, U. Garternicht, and D. Quadfasel (1997), Summer monsoon response of the northern Somali Current, 1995, *Geophys. Res. Lett.*, *24*, 2565–2568.

Shankar, D., and S. R. Shetye (1997), On the dynamics of the Lakshadweep high and low in the southeastern Arabian Sea, *J. Geophys. Res.*, *102*, 551–562.

Shchepetkin, A. F., and J. C. McWilliams (2005), The regional oceanic modeling system (ROMS): A split-explicit, free-surface, topography-following-coordinate oceanic model, *Ocean Modell.*, *9*(4), 347–404, doi:10.1016/j.ocemod.2004.08.002.

Smith, S. L., L. A. Codispoti, J. M. Morrison, and R. T. Barber (1998), The 1994–1996 Arabian Sea expedition: An integrated, interdisciplinary investigation of the response of the northwestern Indian Ocean to monsoonal forcing, *Deep Sea Res., Part II*, *45*(10–11), 1905–1915, doi:10.1016/S0967-0645(98)00058-7.

Takahashi, T., W. S. Broecker, and S. Langer (1985), Redfield ratio based on chemical data from isopycnal surfaces, *J. Geophys. Res.*, *90*, 6907–6924.

Toon, R. K., S. E. Lohrenz, C. E. Rathbun, A. M. Wood, R. A. Arnone, B. H. Jones, J. C. Kindle, and A. D. Weidemann (2000), Photosynthesis-irradiance parameters and community structure associated with coastal filaments and adjacent waters in the northern Arabian Sea, *Deep Sea Res., Part II*, *47*(7–8), 1249–1277, doi:10.1016/S0967-0645(99)00143-5.

Treguier, A., et al. (2001), An eddy-permitting model of the Atlantic circulation: Evaluating open boundary conditions, *J. Geophys. Res.*, *106*, 22,115–22,129.

Van Leer, B. (1979), Towards the ultimate conservative difference scheme, V. A second order sequel to Godunov's method, *J. Comput. Phys.*, *32*, 101–136.

Veldhuis, M. J. W., G. W. Kraay, J. D. L. V. Bleijswijk, and M. A. Baars (1997), Seasonal and spatial variability in phytoplankton biomass, productivity and growth in the northwestern Indian Ocean: The Southwest and Northeast Monsoon, 1992–1993, *Deep Sea Res., Part I*, *44*(3), 425–449, doi:10.1016/S0967-0637(96)00116-1.

Webster, P. J., A. M. Moore, J. P. Loschnigg, and R. R. Leben (1999), Coupled oceanic atmospheric dynamics in the Indian Ocean during 1997–98, *Nature*, *401*, 356–360.

Weller, R. A., A. S. Fischer, D. L. Rudnick, C. C. Eriksen, T. D. Dickey, J. Marra, C. Fox, and R. Leben (2002), Moored observations of upper-ocean response to the monsoons in the Arabian Sea during 1994–1995, *Deep Sea Res., Part II*, *49*(12), 2195–2230, doi:10.1016/S0967-0645(02)00035-8.

Wiggert, J. D., B. H. Jones, T. D. Dickey, K. H. Brink, R. A. Weller, J. Marra, and L. A. Codispoti (2000), The Northeast Monsoon's impact on mixing, phytoplankton biomass and nutrient cycling in the Arabian Sea, *Deep Sea Res., Part II*, *47*, 1353–1385.

Wiggert, J. D., R. G. Murtugudde, and C. R. McClain (2002), Processes controlling interannual variations in wintertime (Northeast Monsoon) primary productivity in the central Arabian Sea, *Deep Sea Res., Part II*, *49*, 2319–2343.

Wiggert, J. D., R. Hood, K. Banse, and J. Kindle (2005), Monsoon-driven biogeochemical processes in the Arabian Sea, *Prog. Oceanogr.*, *65*(2–4), 176–213, doi:10.1016/j.pocean.2005.03.008.

Wiggert, J. D., R. Murtugudde, and J. Christian (2006), Annual ecosystem variability in the tropical Indian Ocean: Results of a coupled bio-physical ocean general circulation model, *Deep Sea Res., Part II*, *53*, 644–676.

Willebrand, J., B. Barnier, C. Böning, C. Dieterich, P. D. Killworth, C. L. Provost, Y. Jia, J.-M. Molines, and A. L. New (2001), Circulation characteristics in three eddy-permitting models of the North Atlantic, *Prog. Oceanogr.*, *48*(2–3), 123–161, doi:10.1016/S0079-6611(01)00003-9.

Young, D. K., and J. C. Kindle (1994), Physical processes affecting availability of dissolved silicate for diatom production in the Arabian Sea, *J. Geophys. Res.*, *99*, 22,619–22,632.

Zhang, Y., W. B. Rossow, A. A. Lacis, V. Oinas, and M. I. Mishchenko (2004), Calculation of radiative fluxes from the surface to top of atmosphere based on ISCCP and other global data sets: Refinements of the radiative transfer model and the input data, *J. Geophys. Res.*, *109*, D19105, doi:10.1029/2003JD004457.

O. Aumont, LPO, CNRS, IRD, BP 70, F-29280 Plouzané, France.

D. Kumar, National Institute of Oceanography, Dona Paula 403004, India.

M. Lévy, G. Madec, S. Pous, and L. Resplandy, LOCEAN, UPMC, BC100, 4 pl. Jussieu, F-75252 Paris CEDEX 05, France. (lrlod@locean-ipsl.upmc.fr)